Research Square

Preprints are preliminary reports that have not undergone peer review.
They should not be considered conclusive, used to inform clinical practice,
or referenced by the media as validated information.

Miro1-dependent mitochondria transfer from cardiomyocytes metabolically controls fibroblast fate to maintain heart homeostasis

Anne-Marie Rodriguez

anne-marie.rodriguez@inserm.fr

INSERM/Sorbonne University https://orcid.org/0000-0001-5557-8975

Jean-Sébastien VARTANIAN-GRIMALDI

Sorbonne University

Zhenlin LI

Sorbonne University

Alexandre Simon

INSERM/ Sorbonne University

Zaven Kabaghian

INSERM/ Sorbonne University

Gabriel Vazquez-Ammirati

INSERM/ Sorbonne University

Gaelle Revet

INSERM/ Sorbonne University

Nathalie Mougenot

2Sorbonne Université, Plateforme PECMV, UMS28

Magali Fradet

Orion Technological Core, CIRB, Collège de France, CNRS, INSERM, Université PSL

Ivan Nemazanyy

Platform for Metabolic Analyses, Structure Fédérative de Recherche Necker, INSERM US24/CNRS UAR 3633 https://orcid.org/0000-0001-8080-839X

Sahna Derni

INSERM/ Sorbonne University

Ara Parlakian

INSERM/ Sorbonne University

Marianne Gervais

Univ Paris Est Créteil, INSERM, IMRB, EnvA, APHP, EFS

Ioannis Xenarios

Swiss Institute of Bioinformatics

Onnik AGBULUT
Sorbonne University

Article

Keywords:

Posted Date: November 6th, 2026

DOI: https://doi.org/10.21203/rs.3.rs-11441111/v1

License: This work is licensed under a Creative Commons Attribution 4.0 International License.
Read Full License

Additional Declarations: There is **NO** Competing Interest.

Miro1-dependent mitochondria transfer from cardiomyocytes metabolically controls fibroblast fate to maintain heart homeostasis

Jean-Sebastien Vartanian-Grimaldi[1,7], Zhenlin Li[1,7], Alexandre Simon[1], Zaven Kabaghian[1], Gabriel Vazquez-Ammirati[1], Gaelle Revet[1], Nathalie Mougenot[2], Magali Fradet[3], Ivan Nemazanyy[4], Sahna Derni[1], Ara Parlakian[1], Marianne Gervais[5], Ioannis Xenarios[6], Onnik Agbulut[1] and Anne-Marie Rodriguez[1,8*]

[1]Institut de Biologie Paris-Seine (IBPS), UMR CNRS 8263, INSERM U1345, Development, Adaptation and Ageing, Sorbonne Université, Paris, France; [2]Sorbonne Université, Plateforme PECMV, UMS28, Paris; [3]Orion Technological Core, CIRB, Collège de France, CNRS, INSERM, Université PSL, Paris, France; [4]Platform for Metabolic Analyses, Structure Fédérative de Recherche Necker, INSERM US24/CNRS UAR 3633, Paris, France; [5]Inserm, IMRB U955-E10, 94000 Créteil, France; Université Paris Est Créteil, Faculté de Santé, 94000 Créteil, France; Ecole Nationale Vétérinaire d'Alfort, 94700 Maisons-Alfort, France; [6]University of Lausanne, Lausanne, Switzerland.

[7]These authors contributed equally

[8]Lead Contact

[*]Correspondance : anne-marie.rodriguez@inserm.fr

ABSTRACT

Recent evidence indicates that mitochondria can move beyond their cell of origin and be internalized by neighboring cells, where they modulate cellular metabolism to influence cell fate. This process, termed intercellular mitochondria transfer, has recently been shown to contribute to tissue homeostasis across several organs. However, whether intercellular mitochondria transfer occurs in the heart and regulates its function remains unclear.

Here, we identify intercellular mitochondria transfer from cardiomyocyte to cardiac fibroblasts as a critical regulator of heart homeostasis. Using complementary *in vivo* and *in vitro* approaches, we showed that cardiomyocytes transfer their mitochondria to cardiac fibroblasts through a Miro1-dependent mechanism and that this process prevents the profibrogenic activation of recipient fibroblasts under homeostatic conditions. Consistent with this finding, cardiomyocyte-specific Miro1 loss-of-function resulted in excessive cardiac fibrosis and impaired contractile function. Mechanistically, mitochondria transfer decreased succinate

levels in recipient fibroblasts by enhancing SDHA expression and mitochondrial complex II activity, thereby inhibiting HIF1α-mediated profibrotic signaling. Finally, intravenous administration of isolated cardiomyocyte-derived mitochondria partially reversed fibroblast activation in mice with cardiomyocyte-specific Miro1 deficiency, further supporting the physiological relevance of mitochondria transfer.

Taken together, our study reveals a novel mechanism by which cardiomyocytes maintain heart homeostasis and opens new therapeutic avenues for preventing cardiac fibrosis, a hallmark of cardiovascular diseases.

INTRODUCTION

Cardiac fibroblasts play a key role in the maintenance of heart homeostasis through the coordinated deposition and remodeling of the extracellular matrix (ECM) to preserve the structural integrity and mechanical function of the heart [1,2]. In response to physiological cues or injury, quiescent fibroblasts differentiate into activated myofibroblasts, characterized by increased proliferation, expression of α-smooth muscle actin (αSMA), and robust secretion of ECM proteins, including collagens and fibronectin. While this phenomenon is essential for physiological remodeling and tissue repair, the persistence of activated myofibroblasts leads to excessive ECM accumulation resulting in pathological cardiac fibrosis, ventricular remodeling and ultimately heart failure [2].

Increasing evidence from various tissues implicates cellular metabolism as a key regulator of fibroblast activity. Indeed, extensive metabolic reprogramming has been reported during the profibrotic activation of fibroblasts, including enhanced glycolysis, altered tricarboxylic acid (TCA) cycle activity and reduced fatty acid β-oxidation [3–5].

Beyond providing energy and building blocks for cellular component synthesis, these metabolic changes also generate metabolites that act as signaling molecules, modulating transcriptional and epigenetic programs that drive fibroblast activation. Among these metabolites, succinate has attracted particular attention as a signaling intermediate involved in fibrosis in various tissues including lung [6,7], liver [8] and kidney [9]. Notably, in a bleomycin-induced model of pulmonary fibrosis, succinate has been shown to accumulate in activated myofibroblasts, where it promotes a profibrotic phenotype by stabilizing HIF1α [7].

Although elevated succinate levels have been reported in the fibrotic heart, and exogenous succinate treatment has been shown to promote cardiac fibroblast activation [10,11], whether succinate contributes to the metabolic reprogramming underlying fibroblast activation remains unclear.

Beyond metabolism , fibroblast activity is also tightly regulated by intercellular communication with neighboring cardiac resident cells, particularly cardiomyocytes, through both paracrine signaling and direct cell–cell interactions [12].

Recently, intercellular mitochondria transfer has emerged as a novel mode of cell-to-cell communication capable of profoundly altering the fate of recipient cells by reprogramming their metabolism [13–17]. Several modalities of mitochondria transfer have been reported classically categorized into contact-dependent and contact-independent routes [14,16]. Among these, the most extensively characterized mechanism is the cell contact-dependent transfer through transient intercellular connections termed tunnelling nanotubes (TNTs), requiring the mitochondrial Rho GTPase Miro1. Mitochondria transfer from cardiomyocytes to fibroblasts via TNTs has been described *in vitro* [18] and, more recently, *in vivo* in a mouse model of sepsis-related cardiac dysfunction [19]. However, whether cardiomyocytes transfer mitochondria to cardiac fibroblasts *in vivo* under physiological conditions, and whether this process regulates the metabolism and the activity of fibroblast, have yet to be determined.

Here, we provide evidence that cardiomyocytes transfer mitochondria to cardiac fibroblasts *in vivo* and demonstrate that this process restrains fibroblast activation pointing to a mechanism involving the prevention of intracellular succinate accumulation and the subsequent stabilization of HIF1α.These findings identify mitochondria transfer as a direct metabolic communication pathway through which cardiomyocytes maintain cardiac homeostasis.

RESULTS

Mitochondria transfer from cardiomyocyte to cardiac fibroblast occurs *in vivo* and *in vitro* and is associated with a less profibrotic phenotype.

To determine whether cardiomyocytes transfer mitochondria to fibroblasts *in vivo*, we generated an inducible transgenic mouse model (CM-Mito$^{GFP)}$ in which cardiomyocyte mitochondria are selectively labeled with GFP following tamoxifen administration. Fourteen days after tamoxifen treatment, healthy hearts were enzymatically dissociated, and fibroblasts were isolated by magnetic sorting (Figure 1A, supplementary figure S1, A). Flow cytometry analysis following GFP staining revealed that approximately 30% of the fibroblast population was GFP-positive, reflecting the uptake of cardiomyocyte-derived mitochondria by these cells (Figure 1B). Consistent with these findings, three-dimensional imaging of cleared hearts from CM-Mito^{GFP} mice confirmed the presence of GFP-positive mitochondria within fibroblasts *in situ* (Figure 1C).

We next examined whether the transfer of cardiomyocyte-derived mitochondria was associated with changes in fibroblast phenotype. To this end, cardiac fibroblasts isolated from CM-Mito^{GFP} hearts were labelled with antibodies against the two profibrotic markers collagen and α-SMA before flow cytometric analysis. We found that GFP-positive fibroblasts expressed lower levels of collagen I and αSMA than GFP-negative counterparts (Figure 1D), indicating that the acquisition of cardiomyocyte-derived mitochondria is associated with a less profibrotic fibroblast phenotype.

To determine whether mitochondria transfer from cardiomyocytes to fibroblasts also occurs in a human context, we established an *in vitro* coculture model using human induced pluripotent stem cell (iPSC)-derived cardiomyocytes transduced with an adenoviral vector expressing mitochondria-targeted DsRed2 and human cardiac fibroblasts labeled with Alexa Fluor 647 conjugated wheat germ agglutinin (WGA).

Following 24 h of coculture, flow cytometry and immunofluorescence analyses showed that almost all cardiac fibroblasts exhibited DsRed2 fluorescence indicating the presence of cardiomyocyte-derived mitochondria (Figure 1E, F, supplementary figure S1, B). Concomitantly, cocultured fibroblasts displayed a markedly attenuated profibrotic phenotype compared with fibroblasts cultured alone, as evidenced by reduced protein expression of collagen I, αSMA and fibronectin (Figure 1G, supplementary figure S1, C).

To further confirm the anti-fibrotic effect of cardiomyocyte mitochondria transfer, human cardiac fibroblasts, which acquire an activated phenotype under standard serum free culture conditions, were preconditioned for 24 h with mitochondria isolated from human cardiomyocytes. Consistent with *in vivo* and coculture findings, fibroblasts internalized cardiac

mitochondria (data not shown) and exhibited significantly reduced protein expression of collagen I, αSMA, and fibronectin (Figure 1H, I).

Taken together, these findings demonstrate that cardiomyocytes transfer mitochondria to fibroblasts in both the mouse heart *in vivo* and in a human *in vitro* model and that this phenomenon is associated with a less fibrotic phenotype in fibroblasts.

Mitochondria transfer from cardiomyocytes to cardiac fibroblasts is primarily mediated by Miro1.

Since the mitochondrial Rho GTPase Miro1 is a key mediator of mitochondria transfer through TNTs [16], we next investigated *in vivo* whether cardiomyocytes use Miro1 to transfer their mitochondria to cardiac fibroblasts. To this end, we generated an inducible double-transgenic mouse model (CM-Mito$^{GFP/Miro1KO}$) in which tamoxifen administration simultaneously induces specific mitochondrial GFP expression and Miro1 loss in cardiomyocytes (Figure 2A).

Fourteen days after tamoxifen treatment, cardiac fibroblasts isolated from CM-Mito$^{GFP/Miro1KO}$ hearts were analyzed by flow cytometry. These experiments revealed that the proportion of cardiac fibroblasts containing cardiomyocyte GFP-positive mitochondria was dramatically reduced in CM-Mito$^{GFP/Miro1KO}$ hearts (6,2% on average) compared with CM-Mito$^{GFP/Miro1WT}$ controls (26.8% on average) (Figure 2B), supporting the critical role of Miro1 in mediating mitochondria transfer from cardiomyocytes to fibroblasts *in vivo.*

We next investigated the expression of profibrotic markers in cardiac fibroblasts isolated from CM-Mito$^{GFP/Miro1KO}$ hearts by flow cytometry. We found that fibroblasts from CM-Mito$^{GFP/Miro1KO}$ hearts exhibited significantly increased expression of collagen I and αSMA compared with fibroblasts from control CM-Mito$^{GFP/Miro1WT}$ hearts (Figure 2C), suggesting that impairment in Miro1-dependent mitochondria transfer promotes fibroblast activation.

To determine whether *vivo* findings could be recapitulated in a human model, we performed coculture experiments using human iPSC-derived cardiomyocytes with Miro1 silencing and DsRed2 mitochondria labeling, together with human cardiac fibroblasts previously stained with Alexa 647-coupled WGA.

After 24 hours, flow cytometry revealed significantly reduced mitochondria transfer from Miro1-silenced cardiomyocytes to cardiac fibroblasts, as indicated by decreased DsRed2

fluorescence in cocultured fibroblasts compared with those from control cardiomyocyte-cocultures (Figure 2D).

We also observed that Miro1-silenced cardiomyocytes lost their antifibrotic effects as shown by the unchanged flow cytometry expression of collagen I, αSMA and fibronectin in cocultured fibroblasts by comparison to control fibroblasts cultured alone (Figure 2E).

Finally, to determine whether paracrine signaling from control or Miro1-silenced cardiomyocytes contributes to the fibroblast phenotype, cardiac fibroblasts were treated for 24 hours with conditioned media collected from either control or Miro1-silenced cardiomyocytes. Both conditioned media induced comparable fibroblast phenotypes, as assessed by flow cytometric analysis of collagen I, αSMA, and fibronectin expression (Figure 2F), indicating that the phenotypic differences between fibroblasts from the two coculture conditions cannot be attributed to paracrine mechanisms.

Collectively, these findings reveal that mitochondria transfer from cardiomyocytes to cardiac fibroblasts is mainly mediated by Miro1 and strengthens that this process prevents fibroblast activation.

Inhibition of Miro1-dependent mitochondria transfer from cardiomyocytes to cardiac fibroblasts is associated with extensive cardiac fibrosis and impaired cardiac function.

To determine the physiological consequences of disrupting Miro1-dependent mitochondria transfer from cardiomyocytes to fibroblasts *in vivo*, we first characterized transcriptional changes in whole hearts from control and CM-Mito^{Miro1KO} mice 14 days after tamoxifen administration by bulk RNA sequencing. This experiment reveals that cardiomyocyte-specific Miro1 deletion altered the expression of 636 genes (438 upregulated and 198 downregulated; fold change >2, q <0.05) (supplementary figure S1, supplementary table S1). Gene Set Enrichment Analysis (GSEA) of differentially expressed genes revealed that the first five most significant enriched gene-sets are associated with fibrosis (Figure 3A, supplementary table S2). Consistent with this, Gene Ontology and Reactome analyses revealed robust enrichment of pathways related to extracellular matrix organization, external encapsulating structure, extracellular matrix structural constituents, collagen biosynthesis and modifying enzymes, and collagen trimer assembly, indicating activation of a profibrotic transcriptional program in cardiomyocyte-specific Miro1-knockout hearts (Figure 3A). Accordingly, more than 20

collagen genes were significantly upregulated following cardiomyocyte Miro1 deletion (Figure 3B).

Additional quantitative RT–PCR validated efficient downregulation of *Miro1* expression and confirmed increased expression of multiple extracellular matrix and profibrotic genes, including *Col1a1*, *Col1a2*, *Col3a1*, *Fn1*, *Ctgf*, *Tgfb1*, *Fap*, and *Mmp2*, in CM-Mito^{Miro1KO} hearts compared with CM-Mito^{MiroWT} controls (Figure 3C). These transcriptional changes were accompanied by a marked increase in interstitial collagen deposition, as assessed by Sirius Red staining, indicative of enhanced cardiac fibrosis in CM-Mito^{Miro1KO} hearts (Figure 3D). xxxxx (supplementary figure S2, supplementary table S3).

We next quantified fibroblast density in control and CM-Mito^{Miro1KO} hearts from bulk cardiac cells exempt of cardiomyocytes. Flow cytometry revealed that CM-Mito^{Miro1KO} hearts exhibited a significantly higher proportion of mEF-SK4-positive fibroblasts than control hearts (31.2% versus 20.2%, respectively, on average Figure 3E), consistent with a pro-fibrotic activation of cardiac fibroblasts when Miro-1 is specifically depleted in cardiomyocytes.

Finally, to determine the consequences of elevated cardiac fibrosis in CM-Mito^{Miro1KO} hearts on cardiac function, we performed echocardiographic analysis at 14 days post tamoxifen administration. CM-Mito^{Miro1KO} mice exhibited profound systolic dysfunction, characterized by a significantly reduced left ventricular ejection which was accompanied by significant increased left ventricular mass (Figure 3F). Accordingly, an elevated heart-to-body weight ratio was observed in CM-Mito^{Miro1KO} mice compared with control littermates (Figure 3G), indicating that the specific loss of Miro1 in cardiomyocytes leads to adverse cardiac remodeling and left ventricular functional decline.

Together, these findings highlight the essential role of cardiomyocyte Miro1 in regulating fibrosis and maintaining cardiac homeostasis.

Mitochondria transfer from cardiomyocytes is associated with metabolic reprogramming and reduced succinate levels in recipient cardiac fibroblasts.

To assess how the transfer of mitochondria from cardiomyocytes modulates recipient cardiac fibroblast metabolism, we performed targeted metabolomic profiling of cardiac fibroblasts harvested from CM-Mito^{Miro1WT} and CM-Mito^{Miro1KO} hearts.

We identified that cardiomyocyte-specific Miro1 deletion altered the expression of 111 metabolites compared to CM-Mito^{Miro1WT} fibroblasts (supplementary figure S3, supplementary table S3).

Among the pathways significantly altered in cardiac fibroblasts from CM-Mito^{Miro1KO} mice, we observed an increase in fatty acid biosynthesis as evidenced by elevated levels of caproic, caprylic, capric, myristic, and palmitic acids, together with enhanced glycolysis, reflected by increased levels of dihydroxyacetone phosphate (DHAP) and phosphoenolpyruvate (PEP) compared with controls hearts (Figure 4A, B, supplementary table S4). In addition, the TCA cycle was significantly altered, with accumulation of several metabolites, including citrate, oxoglutarate, and succinate, in fibroblasts from CM-Mito^{Miro1KO} hearts (Figure 4A, B, C).

We next investigated whether mitochondria preconditioning alters the metabolic profile of human cardiac fibroblasts. We found that 24 hours of preconditioning modified the expression of 133 metabolites (supplementary figure S3, supplementary table S3). Although this *in vitro* model did not fully recapitulate all *in vivo* metabolic shifts, several alterations were conserved. These included decreased caproic acid in lipid metabolism and reduced levels of the glycolytic metabolites DHAP and PEP (Figure 4D, E, supplementary table S4). Furthermore, among the TCA cycle metabolites that exhibited similar profiles to those observed *in vivo*, mitochondria preconditioning significantly reduced succinate levels in human cardiac fibroblasts (Figure 4D, E, F).

We therefore investigated whether succinate was involved in the effects mediated by mitochondria transfer. To this end, cardiac fibroblasts were preconditioned with mitochondria-derived from cardiomyocytes in the presence excess cell-permeable succinate during 24 h. Flow cytometry analysis revealed that succinate supplementation abolished the effects of mitochondria preconditioning on the expression of collagen I, fibronectin and aSMA in recipient fibroblasts (Figure 4G).

Taken together, these *in vivo* and *in vitro* observations strongly suggest that mitochondria transfer from cardiomyocytes suppresses cardiac fibroblast profibrotic activation by decreasing succinate levels.

Mitochondria transfer from cardiomyocytes enhances mitochondrial complex II - dependent respiration in recipient cardiac fibroblasts

Since succinate levels depend on activity of mitochondrial complex II, also known as succinate dehydrogenase (SDH) that catalyzes the oxidation of succinate to fumarate [20], we hypothesized that mitochondria transfer from cardiomyocytes lowers succinate level by increasing mitochondrial complex II activity in recipient cardiac fibroblasts.

To test this hypothesis, we first examined whether the transfer of GFP-positive mitochondria from cardiomyocytes modulated the expression of Complex II subunit A (SDHA) in the cardiac fibroblasts of CM-Mito^{GFP} mice. Flow cytometric analysis revealed that GFP-positive fibroblasts displayed significantly higher SDHA expression compared with their GFP-negative counterparts (Figure 5A). We next compared SDHA expression in fibroblasts from control and CM-Mito^{Miro1KO} hearts by flow cytometry. Fibroblasts from CM-Mito^{Miro1KO} hearts exhibited significantly reduced SDHA expression and increased αSMA levels (Figure 5B), consistent with an inverse relationship between SDHA expression and fibroblast activation in the context of succinate accumulation.

These findings were confirmed in human coculture experiments. Cardiac fibroblasts co-cultured with control cardiomyocytes exhibited increased SDHA expression compared to fibroblasts cultured alone, whereas Miro1-silenced cardiomyocytes failed to induce this response (Figure 5C). Consistent with a direct contribution of mitochondria transfer, exposure of cardiac fibroblasts to isolated cardiomyocyte-derived mitochondria similarly increased SDHA expression (Figure 5D). This induction was abolished in the presence of excess cell-permeable succinate (Figure 5D), supporting the critical role for succinate in mediating the effects of mitochondria transfer.

We next investigated whether mitochondria transfer altered mitochondrial respiration in human cardiac fibroblasts after 24 h exposure to cardiomyocyte-derived mitochondria. Seahorse extracellular flux analysis revealed that mitochondria transfer significantly increased basal and maximal oxygen consumption rates (OCR), whereas ATP-linked respiration displayed a non-significant upward trend. Proton leak was also increased, suggesting an overall enhancement of mitochondrial respiratory consistent with the metabolic shift previously reported in quiescent fibroblasts [21] (Figure 5E, F).

To determine whether increased oxidative capacity and SDHA expression were associated with enhanced succinate oxidation, we performed Seahorse analysis following the sequential addition of rotenone, succinate, and antimycin as previously described [22]. We found that the acquisition of cardiomyocyte mitochondria significantly enhanced Complex II-dependent

respiration in recipient fibroblasts, whereas Complex I-linked oxygen consumption was not significantly altered (Figure 5G, H).

Collectively, these findings suggest that cardiomyocyte-derived mitochondria transfer reduces succinate levels in cardiac fibroblasts by enhancing Complex II-dependent oxidation, evidenced by increased SDHA expression both *in vivo* and *in vitro*, as well as augmented Complex II-linked respiration in the mitochondria-preconditioned fibroblasts.

Mitochondria transfer from cardiomyocytes reduces HIF1α expression in recipient cardiac fibroblasts

To investigate whether cardiomyocyte-to-fibroblast mitochondria transfer modulates fibroblast activity via succinate, we examined the role of HIF1α, a profibrotic transcription factor stabilized by cytosolic succinate accumulation [23].

We first assessed HIF1α expression in cardiac fibroblasts isolated from CM-Mito^{GFP} hearts by flow cytometric analysis following GFP and HIF1α staining. GFP-positive fibroblasts, which had received mitochondria from cardiomyocytes, exhibited significantly lower HIF1α expression than GFP-negative counterparts (Figure 6A), indicating that mitochondria transfer from cardiomyocyte was associated with reduced HIF1α expression in recipient cardiac fibroblasts.

We next compared HIF1α expression level in fibroblasts from CM-Mito^{Miro1WT}and CM-Mito^{Miro1KO} hearts. Flow cytometry analysis revealed increased HIF1α and αSMA expression in fibroblasts from CM-Mito^{Miro1KO} hearts compared with CM-Mito^{Miro1WT} controls (Figure 6B). These findings support the established link between HIF1α expression and fibroblast activation and highlight how cardiomyocytes, through Miro1-dependent mitochondria transfer, can regulate this profibrotic signaling pathway in recipient fibroblasts.

Similarly, flow cytometry analysis revealed decreased HIF1α expression when cardiac fibroblasts were cocultured with human iPSC-derived cardiomyocytes for 24 h compared with fibroblasts cultured alone (Figure 6C). In contrast, coculture with Miro1-silenced cardiomyocytes failed to reduce HIF1α expression in fibroblasts (Figure 6C), suggesting that Miro1-dependent mitochondria transfer contributes to the downregulation of HIF1α expression in recipient fibroblasts.

Furthermore, the impact of mitochondria transfer on HIF1α expression was reinforced by flow cytometry analysis, which showed that preconditioning fibroblasts with cardiomyocyte-derived mitochondria significantly reduced HIF1α protein levels (Figure 6D). Notably, this effect was completely abolished in the presence of excess cell-permeable succinate, indicating that mitochondria transfer modulates HIF1α expression by reducing intracellular succinate levels.

Finally, to validate that HIF1α mediates the antifibrotic effects of mitochondria transfer, cardiac fibroblasts were preconditioned with isolated cardiomyocyte-derived mitochondria in the presence or absence of the HIF1α agonist mimosine.

Pharmacological activation of HIF1α in cardiac fibroblasts abolished the effects of mitochondria preconditioning as shown by the unchanged flow cytometry expression of collagen I, SDHA and HIF1α (Figure 6E), suggesting that HIF1α inhibition is essential for the antifibrotic benefits of mitochondria transfer.

Collectively, these findings suggest that cardiomyocyte-derived mitochondria transfer attenuates cardiac fibroblast activation by inhibiting succinate-dependent HIF1α signaling.

Cardiomyocyte-derived mitochondria transplantation attenuates pro-fibrotic activation of cardiac fibroblasts in $CM^{Miro1KO}$ mice.

To provide additional insights on the role of cardiomyocyte-derived mitochondria transfer in regulating fibroblast activation, we investigated whether systemic transplantation of cardiomyocyte-derived mitochondria could reverse the profibrotic phenotype of cardiac fibroblasts in $CM^{Miro1KO}$ mice. To this end, GFP-positive mitochondria were isolated from CM-$Mito^{GFP}$ hearts two weeks after tamoxifen treatment, when cardiomyocyte mitochondria robustly expressed GFP. Purified GFP-positive mitochondria were administered intravenously beginning 3 days after the final tamoxifen injection and subsequently every 2 days (five injections in total) until CM-$Mito^{Miro1KO}$ mice were sacrificed at day 14 post-tamoxifen administration (Figure 7A). Mitochondria respiration buffer (MRB)injections were used as the vehicle control.

We first determined whether transplanted cardiomyocyte-derived mitochondria were internalized by cardiac fibroblasts in CM-Mito ^{Miro1KO} mice. Immunohistochemical analysis of heart sections from saline- and mitochondria-treated CM-$Mito^{Miro1KO}$ mice using antibodies against GFP and vimentin revealed the presence of GFP positive mitochondria not only within

cardiomyocytes but also in vimentin-positive interstitial cells (Figure7B). Transplanted mitochondria uptake by cardiac fibroblasts was further validated by flow cytometry, which showed slight but significantly increased GFP fluorescence in fibroblasts isolated from mitochondria-treated CM-Mito^{Miro1KO} hearts compared with those from MRB-treated controls (Figure 7C).

We next assessed whether mitochondria transplantation affected the phenotype of cardiac fibroblasts. Flow cytometry analysis demonstrated that transplanted mitochondria reduced the expression of collagen I, αSMA, and fibronectin in cardiac fibroblasts, suggestive of an anti-fibrotic effect (Figure 7C). These phenotypic changes were associated with a trend toward increased SDHA and decreased HIF1α levels (Figure 7D, E)

Taken together, these findings suggest that transplanted cardiomyocyte-derived mitochondria are internalized by cardiac fibroblasts *in vivo* and partially reverse their profibrotic activation, accompanied by shifts in SDHA and HIF1α expression.

DISCUSSION

Our study reveals a novel mechanism of intercellular communication whereby cardiomyocytes modulate fibroblast activity through mitochondria transfer to maintain cardiac homeostasis.

These findings add to the growing body of evidence that intercellular mitochondria transfer is a physiologically relevant mode of communication that enables cells to adapt the functional state of neighboring cells to microenvironmental cues, thereby contributing to tissue homeostasis across diverse organs, including adipose tissue [13,24], brain [25–27] and bone [28]. More specifically, within the heart, cardiomyocytes have been reported to maintain cardiac function by releasing dysfunctional mitochondria via autophagosome-like vesicles, termed exospheres, for clearance by macrophages [29].

Beyond the role of mitochondria transfer to macrophages, our study expands this paradigm, suggesting that these transfer processes appear to be more complex, involving diverse modalities deployed by cardiomyocytes to modulate the activity of other resident cell populations. Specifically, we demonstrate that cardiomyocytes mediate Miro1-dependent mitochondria transfer to cardiac fibroblasts, which acts as a physiological brake on their activation.

While this specific crosstalk and functional consequences in the heart have not been previously reported, some observations from other experimental systems support the anti-fibrotic effect of mitochondria transfer. Notably, mitochondria transplantation has been reported to suppress the activation of extracardiac fibroblasts *in vitro* [30–32] and *in vivo*, in a mouse model of pulmonary fibrosis [32].

Interestingly, recent studies indicate that cardiomyocytes are not the only cell type capable of regulating fibroblast activity through mitochondria transfer. For instance, cancer cells have also recently been shown to exploit this process *in vivo* to promote tumor growth. Notably, mitochondria transfer from cancer cells to fibroblasts has been reported to drive their differentiation into Cancer-Associated Fibroblasts (CAFs) [33] and to enhance chemoresistance[34]. Taken together with our findings in the heart, these data suggest that mitochondria transfer exerts context-dependent effects on fibroblasts, acting as either a beneficial or detrimental mechanism depending on the identity of the donor cell and the surrounding tissue microenvironment.

Adding a further layer of complexity, our study reveals that cardiomyocyte-mediated mitochondria transfer *in vivo* is restricted to a subset of fibroblasts, approximately 30% of the total population, suggesting a highly selective process. Given that single-cell atlases of the mouse and human heart have identified diverse fibroblast subpopulations with distinct molecular profiles and fibrotic capacities [35–38], determining which specific subpopulations preferentially acquire cardiomyocyte-derived mitochondria will be essential to understanding how mitochondria exchanges shape the spatial landscape of fibroblast states within the heart.

Furthermore, our findings identify Miro-1 as a critical regulator of cardiomyocyte-to-fibroblast mitochondria transfer. Although not formally investigated in this study, mitochondria transfer may be mediated by tunneling nanotubes (TNTs), whereby Miro1 interacts with TRAK/Milton adaptor proteins to recruit kinesin and dynein motors, enabling mitochondria to move along the microtubules within TNTs [39]. This hypothesis is consistent with previous *in vitro* studies demonstrating that cardiomyocytes employ TNTs to transfer mitochondria to mesenchymal stem cells [40].

More broadly, the critical role of Miro1 in mediating intercellular mitochondria transfer has been implicated in vivo in the regulation of diverse physiological and pathological processes. including bone homeostasis [15,28], the reparative activity of engrafted mesenchymal stem cells [41–44] and cancer progression [34,45,46]. Notably, lung cancer cells have recently been shown to

transfer mitochondria to cancer-associated fibroblasts (CAFs) through a Miro1-dependent process [34].

Furthermore, our study provides new insights into the metabolic reprogramming triggered by the transfer of cardiomyocyte mitochondria by identifying succinate as a key metabolite, that governs fibroblast fate. Based on our *in vivo* and *in vitro* observations, we propose that mitochondria transfer decreases intracellular succinate levels by stimulating mitochondrial complex II activity, thereby promoting its oxidation into fumarate. Such a decrease may limit its cytosolic accumulation and, consequently, prevent the stabilization of hypoxia-inducible factor-1α (HIF1α) through inhibition of prolyl hydroxylases (PHDs) [23]. Although the succinate/Complex II/HIF1α axis is known to regulate cancer and immune cell behavior [9,47,48] as well as profibrotic activation of lung fibroblasts [7]. its regulation via intercellular mitochondria transfer has not been previously addressed. Our work thus provides an integrated framework connecting mitochondria exchange to metabolic signaling and cardiac homeostasis.

Finally, mitochondria transplantation experiments in mice lacking cardiomyocyte-specific Miro1 provided additional evidence for the antifibrotic properties of cardiomyocyte-derived mitochondria. Notably, we demonstrated that transplanted mitochondria are internalized by cardiac fibroblasts and correlate with a less activated phenotype. This finding offers a new perspective on the interpretation of previous studies reporting beneficial cardiac recovery following mitochondria transplantation [49]. Although current literature largely attributes these improvements to the restoration of cardiomyocyte metabolic and bioenergetic functions [50], our findings suggest that transplanted mitochondria may also exert direct effects on cardiac fibroblasts, thereby contributing to the overall antifibrotic efficacy of this therapeutic strategy.

One of the main limitations of our study is that Miro1 deletion in cardiomyocytes globally alters mitochondria motility, affecting both their intracellular and intercellular trafficking [51,52]. Consequently, the extensive cardiac fibrosis, impaired contractile function and fibroblast phenotype observed *in vivo* following cardiomyocyte-specific Miro1 deletion cannot be attributed solely to impaired cardiomyocyte-fibroblast mitochondria transfer [53]. Nevertheless, our findings provide compelling evidence for a direct antifibrotic role of Miro1-dependent mitochondria transfer as supported *in vivo* by the attenuated profibrotic phenotype of fibroblasts containing cardiomyocyte-derived mitochondria, and *in vitro* by both co-culture and mitochondria preconditioning experiments.

Overall, our study advances the understanding of the communication networks that maintain cardiac homeostasis and opens new therapeutic perspectives for targeting mitochondria transfer to address the ongoing challenge of fibrosis in cardiovascular disease.

FIGURE LEGENDS

Figure 1. Mitochondria transfer from cardiomyocytes counteracts activation of recipient cardiac fibroblasts *in vivo* and *in vitro*.

(A) *In vivo* experimental design.

(B) Representative flow cytometry dot plot showing GFP signal in fibroblast marker (ERTR7)-expressing cells from CM-Mito^{GFP} hearts (upper panel) with quantification (lower panel) (n=14).

(C) Cleared CM-Mito^{GFP} heart showing the presence of GFP-positive mitochondria (green signal) in vimentin-positive fibroblast (red signal, arrow). Scale bar: 20µm.

(D) Representative flow cytometry dot plots of collagen I or αSMA combined with GFP staining in cardiac fibroblasts (upper and lower left panels, respectively), with corresponding relative fluorescence quantification in total population, GFP-positive, and GFP-negative subsets of cardiac fibroblasts (upper and lower right panels, respectively). (Collagen I, n=6; αSMA, n=3).

(E) Representative flow cytometry dot plots of human cardiomyocytes (CM) expressing DsRed2-mitochondria and WGA-labeled cardiac fibroblasts (Fib) cultured alone or in coculture (CC) (left, middle, and right panels, respectively), with DsRed2 fluorescence quantification in single or gated cocultured fibroblasts (right graph) (n=5).

(F) Representative microscopy pictures of cocultures with human cardiomyocytes expressing DSRed2-mitochondria (arrowhead) and WGA-labelled human cardiac fibroblast (arrow). Scale bar: 50µm.

(G) Upper panels: Representative flow cytometry dot plots of SSC-A and cTnT staining in human cardiac fibroblasts cultured alone (Single Fib; left) or in coculture (CC, right). The black rectangle indicates the fibroblast gate. Middle panels: Representative flow cytometry histograms of collagen I, αSMA, and fibronectin in fibroblasts cultured alone (dotted black line)

or in coculture (red filled line). Lower panels: Relative mean fluorescence intensity quantification (n = 6 for collagen I and αSMA, n=5 for fibronectin).

(H) Representative collagen I (green) and αSMA (red) immunostaining in untreated (NT) and mitochondria-treated (+Mito) human cardiac fibroblasts. Hoechst 33342 (blue) labels nuclei. Scale bar, 100 μm.

(I) Upper panels: Representative flow cytometry histograms of collagen I, αSMA, and fibronectin in untreated human cardiac fibroblasts (dotted black line) or mitochondria-treated fibroblasts (red filled line). Lower panels: Relative mean fluorescence intensity quantification (n = 8).

Unpaired Student t-test in (B), Ordinary One-way Anova test in (D). Mann-Whitney test in (E, G, I). * $P < 0.05$, ** $P < 0.01$, *** $P < 0.001$, **** $P < 0.0001$. Each dot represents a single mouse in (B, D) and an independent experiment in (E, G, I). Bar graphs represent mean ± SEM

Figure 2. Miro1 facilitates mitochondria transfer from cardiomyocytes to cardiac fibroblasts and prevents profibrotic activation.

(A) *In vivo* experimental design.

(B) Representative flow cytometry overlay dot plot comparing GFP staining in fibroblast marker (ERTR7)-expressing cells from CM-Mito$^{GFP/Miro1WT}$ (red) and CM-Mito$^{GFP/Miro1KO}$ (blue) hearts (left), with quantification of GFP positive subsets for both mouse groups (right; n = 7).

(C) Representative flow cytometry overlay dot plots of collagen I and αSMA staining in cardiac fibroblasts from CM-Mito$^{GFP/Miro1WT}$ (red) and CM-Mito$^{GFP/Miro1KO}$ (blue) hearts (left), with relative quantification (middle and right panels; n = 9).

(D) Representative flow cytometry overlay dot plots showing human WGA-labeled cardiac fibroblasts (Fib; gray) and cardiomyocytes (CM) expressing mitochondria-targeted DsRed2 (CM; orange) in single cultures (left dot plot), WGA-labeled cardiac fibroblasts in coculture with either untreated cardiomyocytes (CC, middle dot plot; red) or Miro1-silenced cardiomyocytes (CC^{Miro1KD}, right dot plot; blue) by comparison to single culture (gray). Relative DsRed2 fluorescence in cardiac fibroblasts from CC^{Miro1KD} by reference to CC (right panel, n=7).

(E) Upper panels: Representative flow cytometry dot plots of SSC-A and cTnT staining in human cardiac fibroblasts cultured alone (left) or in coculture with Miro1-silenced cardiomyocytes ($CC^{Miro1KD}$). The gate indicates the fibroblast population. Middle panels: Representative flow cytometry histograms of collagen I, αSMA, and fibronectin in fibroblasts cultured alone (dotted black line) or in coculture with Miro1-silenced cardiomyocytes (purple filled line). Lower panels: Relative flow cytometry mean fluorescence quantification in cardiac fibroblasts cocultured with Miro1-silenced human cardiomyocytes ($CC^{Miro1KD}$) by reference to cardiac fibroblasts cultured alone (n = 5).

(F) Representative flow cytometry histograms for collagen I, αSMA, and fibronectin staining in fibroblasts cultured alone (dotted black line) or exposed to conditioned media from either untreated (red filled line, $SN^{control}$) or Miro1-silenced cardiomyocytes (purple filled line, $SN^{Miro1KD}$). Lower panels: Relative flow cytometry mean fluorescence quantification by reference to untreated fibroblasts (n = 4).

Unpaired Student t-test in (B-D), Welch's t test in (E), Kruskal-Wallis test in (F). * $P < 0.05$, ** $P < 0.01$, *** $P < 0.001$, **** $P < 0.0001$. Each dot represents a single mouse in (B, C) and an independent experiment in (D-F). Bar graphs represent mean ± SEM

Figure 3. Deleting Miro1 in cardiomyocytes exacerbates fibrosis and impairs heart function.

(A) Gene Set Enrichment Analysis (GSEA) of genes ranked according to the DESeq2 Wald statistic in hearts from CM-$Mito^{Miro1KO}$ and CM-$Mito^{Miro1WT}$ (Miro-$1^{flox/flox}$) mice (n = 3 per group). The five most enriched gene sets from the GO cellular component (GO:CC), GO molecular function (GO:MF) and Reactome collections are shown. Gene sets are displayed according to their normalized enrichment score (NES), with point size representing gene set size and color representing the Benjamini–Hochberg-adjusted P value (FDR).

(B) Heatmap of collagen genes in CM-$Mito^{Miro1KO}$ and CM-$Mito^{Miro1WT}$ hearts (n = 3 per group). Expression values of genes belonging to the MSigDB GO:CC gene set GOCC_COMPLEX_OF_COLLAGEN_TRIMERS were standardized across samples for each gene to obtain Z-scores. Genes and samples were hierarchically clustered. Sample clustering was performed using Euclidean distance followed by hierarchical clustering.

(C) Quantitative RT-PCR analysis of Miro1 and fibrosis-related genes in the CM-Mito^{Miro1KO} and CM-Mito^{Miro1WT} hearts (n=14 per group except for TGFβ and FAP where n=7 per group).

(D) Representative Sirius Red staining of heart section from CM-Mito^{Miro1KO} and CM-Mito^{Miro1WT} mice (left panels) and stained surface quantification (right panel) (n=8).

(E) Representative flow cytometry dot plots of SSC-A and mEF-SK4 staining of bulk heart cells depleted of cardiomyocytes from CM-Mito^{Miro1KO} and CM-Mito^{Miro1WT} hearts (left panel) and quantification of the percentage of mEF-SK4 positive fibroblasts in both conditions (right panel) (n=8 per group).

(F) Echocardiographic analysis of left ventricular ejection fraction (LVEF, %) and left ventricular (LV, mg) mass in CM-Mito^{Miro1KO} and CM-Mito^{Miro1WT} mice at day 14 post-tamoxifen injection, compared with baseline values at day before tamoxifen treatment (n = 6 CM-Mito^{Miro1WT} mice; n = 10 CM-Mito^{Miro1KO} mice).

(G) Heart-to-body weight ratio (mg/g) for CM-Mito^{Miro1KO} and CM-Mito^{Miro1WT} mice (n = 25 CM-Mito^{Miro1WT} mice; n = 28 CM-Mito^{Miro1KO} mice).

Welch's t test in (C, D), unpaired t-test in (F-G). * $P < 0.05$, ** $P < 0.01$, *** $P < 0.001$. Each dot represents a single mouse. Bar graphs represent mean ± SEM.

Figure 4. Mitochondria transfer from cardiomyocytes leads to decreased succinate levels in recipient fibroblasts.

(A) Enrichment analysis using MetaboAnalyst highlighting dysregulated metabolic pathways in cardiac fibroblasts from CM-Mito^{Miro1KO} hearts compared to CM-Mito^{Miro1WT} (Miro-1$^{flox/flox}$) controls, with particular emphasis on fatty acid biosynthesis, glycolysis and the TCA cycle. The dashed line indicates a raw $P = 0.05$ threshold; pathway impact is shown on the x-axis and bubble size represents the number of metabolite hits.

(B) Heatmap comparing fibroblasts from CM-Mito^{Miro1WT} and CM-Mito^{Miro1KO} hearts of metabolites detected for fatty acid synthesis, glycolysis and TCA (n=3).

(C) Abundance of TCA metabolites in fibroblasts from CM-Mito^{Miro1WT} and CM-Mito^{Miro1KO} hearts (n=3). Z-scores were calculated from log2 transformed metabolite abundances with autoscaling. Means are indicated by diamonds and error bars represent SEM. Two-sided unpaired Welch's *t*-tests. *$P < 0.05$.

(D) Enrichment pathway analysis comparing human untreated and mitochondria-preconditioned cardiac fibroblasts highlighting alterations in fatty acid biosynthesis, glycolysis and the TCA cycle. The dashed line indicates a raw $P = 0.05$ threshold; pathway impact is shown on the x-axis and bubble size represents the number of metabolite hits.

(E) Heatmap showing metabolite profiles associated with fatty acid biosynthesis, glycolysis and the TCA cycle in untreated or mitochondria preconditioned cardiac fibroblasts (n=5).

(F) Abundance of TCA cycle metabolites in untreated or mitochondria preconditioned cardiac fibroblasts (n=5). Each dot represents one independent experiment. Means are indicated by diamonds and error bars represent SEM. Z-scores were calculated from log2 transformed metabolite abundances with autoscaling. Two-sided unpaired Welch's *t*-tests. $*P < 0.05$, $***P < 0.001$.

(G) Representative flow cytometry histograms of collagen I, fibronectin and αSMA staining in untreated or mitochondria-treated fibroblasts in presence of succinate (brown dotted and orange filled lines, respectively) by reference to control fibroblasts cultivated in absence of mitochondria and succinate (black dotted lines) (upper panel) and relative fluorescence quantification by reference to control fibroblasts (NT, lower panel) (n=8).

Ordinary One-way Anova test in (G), $* P < 0.05$, $*** P < 0.001$. Each dot represents mixture sample from 3 mice in (A-C) and an independent experiment in (D-F). Bar graphs represent mean ± SEM

Figure 5. Mitochondria transfer from cardiomyocytes enhances mitochondria complex II expression in recipient cardiac fibroblasts.

(A) Representative flow cytometry dot plot of SDHA and GFP staining in cardiac fibroblasts isolated from CM-Mito^{GFP} (left panel) and quantification of the relative SDHA mean fluorescence in GFP-positive and GFP-negative fibroblast subsets by reference to the total population (n=6).

(B) Representative flow cytometry overlay dot plot of SDHA and αSMA staining in cardiac fibroblasts from CM-Mito^{Miro1WT} (Miro-1$^{flox/flox}$) (red) and CM-Mito$^{GFP/Miro1KO}$ (blue) hearts (left panel), with relative SDHA fluorescence quantification in CM-Mito^{Miro1KO} fibroblasts by reference to CM-Mito^{Miro1WT} controls (right panel; n = 6).

(C) Representative flow cytometry histograms of SDHA staining in fibroblasts cultured alone (dotted black line) or cocultured with either untreated (red filled line) or Miro1-silenced cardiomyocytes (purple filled line) and quantification of relative SDHA flow cytometry by reference to fibroblasts cultured alone (n = 6).

(D) Representative flow cytometry histograms of SDHA staining in untreated (NT, black dotted line) or mitochondria-treated fibroblasts (+Mito, red filled line, up part of left panel) and in presence of succinate (Suc, brown dotted and Suc+Mito, orange filled lines, down part of left panel) and relative SDHA fluorescence quantification (right panel) (n = 9).

(E) Oxygen consumption rate (OCR) assessed in untreated (NT) or mitochondria-treated (+Mito) human cardiac fibroblasts. After the evaluation of basal respiration, oligomycin (OligoA), FCCP and rotenone/antimycin A (ROT/AA) were added as shown to measure the different respiratory parameters.

(F) Quantification of basal respiration, ATP-linked respiration, proton leak, and maximal respiration of untreated (NT) or mitochondria-treated (+Mito) human cardiac fibroblasts (n = 18).

(G) OCR assessed in untreated (NT) and mitochondria-treated (+Mito) human cardiac fibroblasts following sequential addition of rotenone, succinate, and antimycin to assess mitochondrial respiratory complex I and complex II activities.

(H) Mitochondrial complex I- and II-dependent respiration in untreated (NT) and mitochondria-treated (+Mito) human cardiac fibroblasts (n=10).

Ordinary One-way Anova test in (A, D), Kruskal-Wallis test in (C), unpaired t-test in (B, F, H). * $P < 0.05$, ** $P < 0.01$, *** $P < 0.001$, **** $P < 0.0001$. Each dot represents a single mouse in (A, B) and an independent experiment in (D, F, H). Bar graphs represent mean ± SEM

Figure 6. Mitochondria transfer from cardiomyocytes decreases HIF1α expression in recipient fibroblasts.

(A) Representative flow cytometry dot plot of HIF1α and GFP staining in cardiac fibroblasts isolated from CM-Mito^{GFP} hearts (left panel) and quantification of relative HIF1α fluorescence in GFP-positive and GFP negative fibroblast subsets by reference to the total fibroblast population (n=7).

(B) Representative flow cytometry overlay dot plot of HIF1α and αSMA staining in cardiac fibroblasts from CM-Mito^{Miro1WT} (Miro-1$^{flox/flox}$) (red) and CM-Mito^{Miro1KO} (blue) hearts (left panel), with relative HIF1α fluorescence quantification in CM-Mito^{Miro1KO} fibroblasts by reference to CM-Mito^{Miro1WT} fibroblasts (right panel; n = 5).

(C) Representative flow cytometry histograms of HIF1α staining in fibroblasts cultured alone (Alone, dotted black line) or cocultured with either untreated (CC, red filled line) or Miro1-silenced cardiomyocytes (CC^{Miro1KD}, purple filled line) and quantification of relative HIF1α fluorescence by reference to untreated fibroblasts (n = 6).

(D) Representative flow cytometry histograms of HIF1α staining in untreated or mitochondria-treated fibroblasts in absence (NT, black dotted and +Mito, red filled lines, respectively) or presence of succinate (Suc, brown dotted and Suc+Mito, orange filled lines, respectively) (right panel) and relative HIF1α fluorescence quantification (right panel) (n = 9).

(E) Representative flow cytometry histograms showing collagen, SDHA, and HIF1α staining in untreated or mitochondria-treated fibroblasts in the presence of the HIF1α agonist mimosine (Mimo, dotted purple and Mimo+Mito, pink-filled lines, respectively). Untreated fibroblasts cultured in the absence of mimosine are shown as a dotted black line. Relative fluorescence for each marker by reference to control untreated fibroblasts (NT) (right panels; n = 5).

Ordinary One-way Anova test in (A), Mann-Whitney test in (B), Kruskal-Wallis test in (C, D, E). * $P < 0.05$, ** $P < 0.01$, *** $P < 0.001$. Each dot represents a single mouse in (A, B) and an independent experiment in (C, D, E). Bar graphs represent mean ± SEM.

Figure 7 Cardiomyocyte-derived mitochondria transplantation attenuates pro-fibrotic activation of fibroblasts.

(A) *In vivo* experimental design.

(B) Representative immunohistochemical staining for vimentin (red) and GFP in heart sections from CM-Mito^{Miro1KO} mice following tail-vein injection of either mitochondria from CM-Mito^{GFP} hearts or mitochondria respiration buffer (MRB). Merged images have been enlarged for better visibility. Yellow arrowheads indicate cardiomyocytes containing transplanted GFP-positive mitochondria, and white arrows indicate fibroblasts containing transplanted GFP-positive mitochondria. Hoechst 33342 (blue) labels nuclei. Scale bar, 5 μm.

(C) Representative flow cytometry overlay dot plots showing GFP staining in combination with collagen I, αSMA, or fibronectin in cardiac fibroblasts from MRB-treated (pink) or mitochondria-treated (blue) CM-Mito^{Miro1KO} mice (upper panels), and quantification of relative fluorescence for each marker by reference to the MRB-treated group (lower panels; n = 11(MRB-treated) or n=12 (Mitochondria-treated)).

(D) Representative flow cytometry overlay dot plot showing GFP staining in combination with SDHA in cardiac fibroblasts from MRB-treated (pink) or mitochondria-treated (blue) CM-Mito^{Miro1KO} mice (right panel), and relative fluorescence quantification (left panel; n = 11(MRB -treated) or n=12 (Mitochondria-treated)).

(E) Representative flow cytometry overlay dot plot showing GFP staining in combination with HIF1α in cardiac fibroblasts from HBSS-treated (pink) or mitochondria-treated (blue) CM-Mito^{Miro1KO} mice (right), and relative fluorescence quantification (left panel; n = 11 for MRB-treated group and n = 12 for Mitochondria-treated group).

Unpaired t-test in (C, E); Welch's t test in (D). * $P < 0.05$, ** $P < 0.01$. Each dot represents a single mouse. Bar graphs represent mean ± SEM.

MATERIALS AND METHODS

Generation of transgenic CM-Mito^{GFP}, CM-Mito^{Miro1KO} and CM-Mito$^{GFP/Miro1KO}$ mice

Three mouse parental strains: (1) Miro-1$^{flox/flox}$ (strain #:031126) carrying *loxP*-flanked exon 2 of the *Rhot1* (*Miro1*) gene, (2) Mito-EGFP$^{flox/flox}$ (strain #:021429**)** carrying a Cre-dependent mitochondrial GFP reporter, (3) αMHC^{MerCreMer} (strain #:005657) mice expressing the tamoxifen-inducible Cre recombinase MerCreMer under the cardiomyocyte-specific α-myosin heavy chain (Myh6) promoter, were purchased from Jackson Laboratory, Bar Harbor, ME, USA. Both Miro-1$^{flox/flox}$ and Mito-EGFP$^{flox/flox}$ mice were crossed with αMHC^{MerCreMer} mice to obtain double or triple transgenic mice (Miro-1$^{flox/flox}$/αMHC^{MerCreMer}, mito-EGFP$^{flox/+}$/αMHC^{MerCreMer}, or Miro-1$^{flox/flox}$/ mito-EGFP $^{flox/+}$/ αMHC^{MerCreMer}) to generate cardiomyocyte-specific KO of Miro1 (CM-Mito^{Miro1KO}), cardiomyocyte-specific expression of eGFP in mitochondria (CM-Mito^{GFP}) and cardiomyocyte-specific KO of Miro1 and mitochondrial expression of GFP (CM-Mito$^{GFP/Miro1KO}$), respectively, after tamoxifen injection. These mice were injected intraperitoneally with 1 mg of tamoxifen in 100 µL of peanut oil for 3 days. Miro1$^{flox/flox}$ or mito-EGFP $^{flox/+}$ or Miro1$^{flox/flox}$/ mito-EGFP $^{flox/+}$ littermates injected for

3 days with tamoxifen were used as controls. All mice were genotyped by PCR with specific primers (Miro^{Flox}Fw: 5'-AAATGCCACCAGAATCCAGT-3, Miro^{flox}Rev: 5-GTAGCCCAGTATGATGGCACA-3' for Miro-1$^{flox/flox}$ mice; MtGFPCom FW: 5'-CTTCCCTCGTGATCTGCAAC-3', MtGFP^{flox}Rev: 5'-GTTATGTAACGCGGAACTCCA-3', MtGFPWTRev: 5'-CAGGACAACGCCCACACA-3' for Mito-EGFP$^{flox/flox}$ mice; MHCPRO: CTCTGACAGAGAAGCAGGCAC, MERR: CGCCAGACGAGACCAATCATCA for αMHC^{MerCreMer} mice.

Mouse sex, age and ethical considerations.

Mice of both sexes, aged 3–6 months, were used for the experiments. Mice were housed in a temperature- and humidity-controlled facility with a 12h light/day cycle and given free access to standard rodent chow and water. All animal procedures were performed in accordance with the French regulations and the experimental guidelines of the European Community and the protocols were approved by the local Animal Ethics Committee (#37927) of the Sorbonne University, Paris, France. All mice were killed by cervical dislocation 14 days post-tamoxifen treatment.

Human primary cardiac fibroblasts.

Primary human ventricular cardiac fibroblasts (NHCF-V; Lonza, Cat#CC-2904) were expanded in fibroblast growth medium-3 (FGM-3; Lonza) and used between passages 8 and 10.

Culture of human induced pluripotent stem cells (hiPSCs) and differentiation into cardiomyocytes.

The iPSC line (EPI) used in this study were purchased from ThermoFisher Scientific and declared by the Sorbonne University for the conservation and preparation of human body elements for the needs of research programs (CODECOH) to the Ministry of Higher Education, Research and Innovation (Approval number: DC-2024-6723).

The iPSCs were grown on Matrigel-coated dishes (Corning) in mTeSR+ medium (STEMCELL Technologies). At 80% confluence, cells were detached using ReLeSR (STEMCELL Technologies) and replated at a 1:30 split ratio according to the manufacturer's instructions.

Differentiation of hiPSCs into cardiomyocytes was assessed by sequential modulation of Wnt signaling, as previously described, with minor modifications [54]. Briefly, hiPSCs were cultured in RPMI supplemented with 2% insulin-free B27 (Gibco, Cat#A18956-01).

and 9 µM CHIR99021 (Tocris-Bioscience, Cat#4423/10) for 24 hours. Cells were then maintained for 2 days in RPMI supplemented with 2% insulin-free B27, followed by a further 2 days in the same medium supplemented with 5 µM IWP2 (Tocris-Bioscience, Cat# 3533/10). After that, cells were cultivated in RPMI / 2% B27 containing insulin (Gibco, Cat# 17504-044), with medium changes every other day until day 30. Cells were then dissociated, passed through a 70-µm cell strainer and cryopreserved in PSC Cryomedium (Life Technologies) to establish a homogeneous cardiomyocyte bank.

Human cardiac RL-14 Cell Line.

The human fetal ventricular cardiomyocyte RL14 cell line was purchased from the American Type Cell Culture (ATCC, LGC Standards S.a.r.l. Molsheim France). RL14 cells were grown in DMEM/F-12 (Life technologies) supplemented with 10% heat inactivated FBS, 100 U/ml penicillin, 100 µg/ml streptomycin, and 10 mM HEPES [55].

Coculture of human iPSC-derived cardiomyocytes and primary human cardiac fibroblasts.

Human iPSC-derived cardiomyocytes and cardiac fibroblasts were thawed 5 and 3 days, respectively, prior to co-culture. Cocultures were performed by seeding cardiac fibroblasts onto adherent cardiomyocytes at a 1:1 ratio, with each cell type seeded at 75000cells /cm². Co-cultures were maintained for 24 h in cardiomyocyte culture medium consisting of RPMI 1640 (Gibco, Cat#21875-034) supplemented with 2% B27 containing insulin (Gibco, Cat#17504-044), 100 U/ml penicillin and 100 µg/ ml streptomycin (Gibco, Cat#15140-122) before downstream analyses.

To label mitochondria, cardiomyocytes were transduced with the adenoviral vector Ad-Mito-DsRed2 (SL100744; Signagen Laboratories, Frederick, MD, USA), which contains the mitochondrial targeting sequence derived from subunit VIII of human cytochrome c oxidase (Mito) fused to the N-terminus of DsRed2 at MOI 10 :1.

To knock-down the expression of Miro1 (Rhot1) in cardiomyocytes, cells were transduced with the adenoviral vector Ad-U6-Miro1shRNA-EGFP (VectorBuilder, Chicago, IL, USA) at MOI 10 :1. Known-down efficiency (around 90%) of Miro1 gene expression was confirmed by RT-qPCR. Adenoviral vector containing scramble shRNA that does not recognize any sequence in the human genome from VectorBuilder was used as a negative control.

Both adenoviral infections were performed on cardiomyocytes 3 days prior the coculture.

Mitochondria transfer assessment in coculture.

To visualize mitochondria transfer, human iPSC-derived cardiomyocytes previously transduced with the adenoviral vector Ad-Mito-DsRed2 were cocultured with cardiac fibroblasts previously stained with Alexa Fluor 647-conjugated wheat germ agglutinin (WGA) (5 µg/ml; Invitrogen, Cat#W32466) during 24 h, after which cells were fixed in 4% paraformaldehyde for 10 min. Images were acquired using a Leica DMi8 microscope equipped with a digital camera (Leica Microsystems, Nanterre, France).

To quantify mitochondria transfer, similar coculture experiments were performed and analysed by flow cytometry (Cytoflex LX, Beckman Coulter). Mitochondria transfer was assessed by measuring DsRed fluorescence in WGA-stained cardiac fibroblasts (supplementary figure S1, B).

To assess the involvement of Miro1 in mitochondria transfer, human iPSC-derived cardiomyocytes were transduced with both the adenoviral vector Ad-Mito-DsRed2 and the adenoviral vector Ad-U6-Miro1shRNA-EGFP (each at MOI: 10:1). Transduced cardiomyocytes were subsequently cocultured with cardiac fibroblasts stained with Alexa Fluor 647-conjugated WGA during 24 hours. DsRed fluorescence in cardiac fibroblasts was then analyzed by flow cytometry (supplementary figure S1, B).

Cardiomyocyte conditioned media exposure to cardiac fibroblasts.

Conditioned media from scramble or Miro1-silenced cardiomyocytes cultured alone for 24 h were collected and added to fibroblasts for 24 h prior flow cytometry experiments.

Mitochondria isolation from RL14 cells and mitochondria preconditioning of human primary cardiac fibroblasts.

Mitochondria were isolated from human RL14 cells using the Mitochondria Isolation Kit (Thermo Scientific, Cat# 89874) according to the manufacturer's instructions, with the final centrifugation performed at 3,000 x g. The concentration of mitochondrial proteins was determined using the bicinchoninic acid (BCA) assay (Pierce™ BCA Protein Assay Kit, Thermo Scientific, Cat# 23227).

Cardiac fibroblasts, seeded 20000 cells/cm^2, were exposed to isolated mitochondria at a concentration corresponding to 100 µg of mitochondrial protein per 10^5 cells in serum free DMEM high glucose with glutamine and sodium Pyruvate (Gibco, Cat# 41966-029) for 24 h.

In some experiments, cardiac fibroblasts were treated with Diisopropyl succinate (5 mM, Sigma-Aldrich, Cat# CDS013595) or Mimosine (400 µM, MedChemExpress, Cat# HY-N0928) during mitochondria preconditioning.

Mitochondria preconditioned cardiac fibroblast immunostaining.

Following 24 hours exposure to RL14-derived mitochondria, human cardiac fibroblasts were fixed with 4% PFA and stained with antibodies against AF647 conjugated collagen I (1:100; Bioss, Cat#BS-10423R-BF647) and unconjugated mouse anti-αSMA (1:100; R&D Systems, Cat# MAB1420). Samples were then exposed to AF568 goat anti-mouse IgG2a secondary antibody (1:100, Invitrogen, Cat# A21134). Nuclei were counterstained with DAPI. Fluorescence was analyzed with a Leica DMi8 microscope.

Mitochondria isolation from CM-Mito^{GFP} hearts.

Heart mitochondria were isolated by differential centrifugation followed by Percoll density-gradient purification, as previously described [56].

Briefly, freshly excised hearts were minced and digested in ice-cold isolation medium (IM) containing 0.5% fatty acid-free bovine serum albumin (BSA), 225 mM sucrose, 75 mM mannitol, 1 mM EGTA and 5 mM HEPES, supplemented with Nagarse (2 mg/ml; Sigma-Aldrich, Cat#P8038). The tissue was subsequently homogenized using a Dounce homogenizer (7–10 strokes) and centrifuged at 1,000g for 5 min to remove cellular debris and nuclei. The resulting supernatant was collected and centrifuged at 12,000g for 10 min to obtain the crude mitochondrial pellet.

The pellet was resuspended and purified by ultracentrifugation at 35,000 g for 10 min at 4 °C without braking) through a discontinuous Percoll density gradient consisting of 18%, 30% and 70% Percoll layers. The mitochondrial fraction was collected from the interface between the 30% and 70% Percoll layers and washed by centrifugation to remove residual Percoll. The final mitochondrial pellet was resuspended in mitochondria respiration buffer (MRB) containing 250 mM sucrose, 20 mM K-HEPES (pH 7.2), 10 mM $MgCl_2$, 500 µM K-EGTA (pH 8.0) and 2 mM KH_2PO_4.

Mitochondrial protein concentration was determined using the bicinchoninic acid (BCA) assay (Pierce BCA Protein Assay Kit, Thermo Scientific, 23227).

Quality Control of isolated Mitochondria.

Mitochondrial membrane integrity was assessed to confirm the functional integrity of the isolated mitochondria, following isolation from RL14 cells or mouse hearts.

Outer mitochondrial membrane integrity was evaluated by measuring Cytochrome C Oxidase activity using the Cytochrome C Oxidase Assay Kit (Abcam, Cat# ab239711), according to the manufacturer's instructions.

Inner mitochondrial membrane integrity was assessed by measuring mitochondrial membrane potential using JC-1 dye. 5 µg of isolated mitochondria was diluted in assay buffer containing 100 mM MOPS (pH 7.5), 550 mM KCl, 50 mM ATP, 50 mM $MgCl_2$, 50 mM sodium succinate, and 5 mM EGTA. JC-1 was added to a final concentration of 0.2 µg/ml Sigma-Aldrich, Cat#420200). Fluorescence was measured at an excitation and emission wavelength of 490 and 590 nm respectively for 10 min using a TECAN Infinite F500 microplate reader.

***In vivo* mitochondria transplantation in CM-Mito^{Miro1KO} mice.**

Fluorescently GFP^+ labeled mitochondria were isolated from the hearts of CM-Mito^{GFP} mice, 14 days after tamoxifen administration. Immediately following isolation, mitochondria were administered intravenously in the tail vein of CM-Mito^{Miro1KO} mice at a dose of 100 µg mitochondrial protein per mouse, diluted in 100 µL of MRB. A total of five mitochondria injections were performed at 2-day intervals, from day 5 to day 13 following tamoxifen administration. As controls, CM-Mito^{Miro1KO} mice received an equivalent volume of MRB alone at the same point. At day 14 after tamoxifen administration, mice were euthanized, and hearts were collected for immunohistochemical analysis or isolation of cardiac fibroblasts.

Cardiac fibroblast isolation.

Cardiac fibroblast were isolated through enzymatic digestion of mouse hearts as previously reported [57] with minor modification followed by magnetic column purification.

Briefly, mice were anesthetized with 5% isoflurane and hearts were collected following thoracotomy, exsanguination by transection of the inferior vena cava and perfusion through the right ventricle with 5 ml warm sterile EDTA buffer (5 mM EDTA, 130 mM NaCl, 5 mM KCl, 0.5 mM NaH_2PO_4, 10 mM HEPES, 10 mM Glucose, 10 mM BDM, 10 mM Taurine, 1 mM $MgCl_2$).

Hearts were minced in buffer containing 0.5mg/ml collagenase 2, 0.5mg/ml collagenase 4 and 0.05mg/ml protease XIV) and digested for 40 min at 37 °C with gentle agitation. Tissue was triturated and filtered through a 100-µm strainer. Digestion was stopped with 5 ml STOP buffer (130 mM NaCl, 5mM KCl, 0.5 mM NaH_2PO_4, 10 mM HEPES, 10 mM Glucose, 10 mM BDM, 10 mM Taurine, 1 mM MgCl2, 5% fetal calf serum). Following two 30-min sedimentation

steps, the supernatant was sequentially filtered through 70- and 40-µm strainers and centrifuged at 300 × g.

Fibroblasts were enriched using the Feeder Removal MicroBeads kit (Miltenyi, Cat#130-095-531) according to the manufacturer's instructions. Briefly, cells were labeled with mEF-SK4-conjugated microbeads and applied to an LS magnetic column (Miltenyi Biotec, Cat#130-042-401) on a magnetic separator. After two washes, mEF-SK4-positive cells corresponding to fibroblasts were eluted from the column with 1 ml culture medium, repeated twice.

Echocardiography.

At day 0 and day 14 after tamoxifen administration, left ventricular dimensions and volumes were assessed in control and CM-Mito^{Miro1KO} mice by transthoracic echocardiography using a VEVO 3100 system (FUJIFILM VisualSonics) equipped with an MX550D probe (25–55 MHz). Mice were anesthetized with isoflurane (2% induction; 0.5% maintenance) during image acquisition. Measurements were obtained in triplicate from digital loops using the M-mode–derived corrected cube formula. Data were analyzed using Vevo LAB software by investigators blinded to experimental groups.

Heart Histology and Immunohistochemistry.

After mouse sacrifice, hearts were embedded in OCT compound (Tissue-Tek, Cat#4583) and immediately snap-frozen in liquid nitrogen–cooled isopentane. Cardiac sections (8 µm thick) were then prepared using a cryostat (Thermo Fisher Scientific).

For assessment of cardiac fibrosis, heart sections were fixed in 4% paraformaldehyde (PFA) and stained with 0.3% Sirius Red (Sigma-Aldrich, Cat# 365548) for 1 h, followed by rapid washing in acetic acid. Sections were mounted in Eukitt (Chem-Lab, Cat# CL04.0503.0500) and imaged by bright-field microscopy using a Leica DMi8 microscope equipped with a digital camera. The area of Sirius Red-positive staining was quantified using ImageJ software and expressed as a percentage of the total tissue area.

For immunohistochemistry, frozen heart sections were fixed in 4% paraformaldehyde for 15 min and blocked for 1 h in PBS containing 5% bovine serum albumin (BSA). Sections were then incubated overnight at 4 °C with goat anti-GFP (1:500; Invitrogen, Cat#PA5-143588) and guinea pig anti-vimentin (1:100; Progen, cat. no. GP53) primary antibodies diluted in PBS containing 2.5% BSA. Following three washes in PBS, sections were incubated for 1 h with Alexa Fluor 488 (AF488)-conjugated rabbit anti-goat IgG (1:400; Invitrogen, Cat#A11078) and AF594-conjugated goat anti-guinea pig IgG (1:400; Invitrogen, Cat#A11076) secondary

antibodies. Nuclei were counterstained with 4′,6-diamidino-2-phenylindole (DAPI) for 5 min, and sections were mounted in Mowiol (Sigma-Aldrich). Images were acquired using a Leica DMi8 microscope equipped with a digital camera (Leica Microsystems, Nanterre, France).

Cardiac muscle clearing for 3D imaging.

Left ventricular biopsies from CM-Mito^{GFP} mice were harvested and immediately fixed in 4% PFA for 2h at 4°C. Biopsies were washed three times with PBS for 10 min at RT and permeabilized with 2% Triton-X 100 in PBS overnight at RT. All the immunostaining steps were performed in dark conditions, at 37°C under agitation at 10 rpm. Cardiac biopsies were incubated with primary chick anti-GFP (1:500; Abcam, Cat#Ab13970) and guinea-pig anti-vimentin (1:200; Progen, Cat#GP53) antibodies diluted in PBS added with 1% goat serum, 0.2% Triton-X 100 and 0.2% sodium azide for 5 days. Samples were rinsed three times with PBS for at least 1 h at RT, under agitation. Samples were then incubated with secondary Alexa 488 anti-chicken (1:500; Invitrogen, Cat#A32931TR) and Alexa 555 anti-guinea pig (1:500; Invitrogen, Cat#A-21435) antibodies for 2 days. For the last 2 h, 4′,6-diamidino-2-phenylindole (DAPI; 1:500, Sigma) was added. After four washes of minimum 1 h at RT, samples were processed for tissue clearing by incubation with RapiClear® 1.52 reagent (Nikon, France) for 12 h. Imaging was performed with a spinning disc microscope (CSU-W1 Leica) using a 25× objective (HCX IRAPOL 25×/0.95 W Leica). Reconstructions (3D) were performed using Imaris 9.5.

Flow cytometry analysis on cardiac fibroblasts from mouse hearts.

For fibroblast quantification in mouse hearts, bulk cardiac cells depleted of cardiomyocytes were isolated from control and CM-Mito^{Miro1KO} hearts at day14 after tamoxifen treatment. Cells were stained with ViaKrome 808 Fixable Viability Dye (0.5µl per 10^6 cells; Beckman Coulter, Cat#C36628) and fixed using Flow Cytometry Fixation Buffer (R&D Systems, Cat#FC004) prior incubation with APC-conjugated anti-mEF-SK4 antibody (10 µl per 10^6 cells; Miltenyi Biotec, Cat#130-120-802) diluted in Flow Cytometry Permeabilization/Wash Buffer I (R&D Systems, Cat#FC005).

For phenotypic characterization, mouse cardiac fibroblasts were similarly stained with ViaKrome 808 Dye and fixed prior staining with fluorochrome-conjugated primary antibodies, used in different combinations according to the experimental requirements. Primary antibodies include AF488 anti-GFP (1:50; R&D Systems, Cat# FAB42402G), APC anti-mEF-SK4 (10 µl per 10^6 cells; Miltenyi Biotec, Cat#130-120-802), AF350-anti-fibroblast

antibody (ER-TR7) (10 µl per 10^6 cells, Novus Biologicals, Cat# NB100-64932AF350), anti-collagen I conjugated to AF647 (1:100; Biossor, Cat#BS-10423R-BF647) or Cy5.5 (1:100; Antibodies online, Cat#ABIN2173317), αSMA conjugated to APC (clone 1A4; 1:50; R&D Systems, Cat#IC1420A) or AF488 (clone 1A4; 1:50; Invitrogen Cat # 53-9760-82), APC anti-fibronectin (clone HFN7.1; 1:50; Novus, Cat#NBP2-34633), anti-HIF1α (clone Mgc3), conjugated to either PE (1:20; Invitrogen, Cat#12-752-882) or APC (1:20; Invitrogen, Cat#17-7528-82), unconjugated anti-SDHA (clone JM10-83; 1:150; Invitrogen, Cat#MA5-32598) detected by AF647 conjugated donkey anti-rabbit IgG (1:100; Interchim, Cat# FP-SC5110) or AF750 goat anti-rabbit IgG (1:100; Invitrogen, Cat# A-21039).
Fluorescence analysis was done on Cytoflex LX flow cytometer (Beckman Coulter) (supplementary figure S1, A). For GFP and MEF-SK4 staining, the positive cell number was quantified. For the other markers, the relative expression of each marker was obtained by the ratio of mean fluorescence of the samples of interest by reference to the control group.

Flow cytometry data were analyzed using FlowJo software v.10.

Flow cytometry analysis on human cardiac fibroblasts following coculture or mitochondria-preconditionning.

Cocultured cells were fixed using Flow Cytometry Fixation Buffer (R&D Systems, Cat#FC004) and stained with PE-conjugated cardiac troponin (cTnT) (clone REA400 /1C11; 1:50; Miltenyi, Cat# 130-120-405) in combination with one of the following antibodies: AF647 anti-collagen I (1:100; Biossor, Cat#BS-10423R-BF647), APC-conjugated αSMA (clone 1A4; 1:50; R&D Systems, Cat#IC1420A), APC-conjugated anti-fibronectin (clone HFN7.1; 1:50; Novus, Cat#NBP2-34633), APC-conjugated anti-HIF1α (clone Mgc3; 1:20; Invitrogen, Cat#17-7528-82), unconjugated anti-SDHA (clone JM10-83; 1:150; Invitrogen, Cat#MA5-32598) detected by AF647 conjugated donkey anti-rabbit IgG (1:100; Interchim, Cat#FP-SC5110).
Mitochondria-preconditioned cardiac fibroblasts were processed similarly to the coculture experiments, except that cardiac troponin T staining was omitted. Data were collected with a MACSQuant Analyser, Miltenyi Biotech).
The relative expression of each marker was obtained by the ratio of mean fluorescence by reference to untreated fibroblasts (supplementary figure S1, C).
Flow cytometry data were analyzed using FlowJo software v.10.

Real-time PCR assays.

Total RNA was isolated from whole hearts of control and CM-Mito^{Miro1KO} mice at day 14 after tamoxifen administration using TRIzol reagent (Invitrogen, Cat#15596018) according to the manufacturer's instructions. One microgram of RNA was reverse-transcribed using the RevertAid First Strand cDNA Synthesis Kit (Thermo Fisher Scientific, Cat#K1622) with random hexamer primers. qPCR was performed in triplicate using Go Taq (R) qPCR Master Mix (Promega, Cat#A6002) and a CFX Opus 384 Real-Time PCR System (Bio-Rad). Cycling conditions were 95 °C for 5 min, followed by 40 cycles of 95 °C for 15 s, 60 °C for 15 s and 72 °C for 30 s. Hydroxymethylbilane synthase (Hmbs) was used as the reference gene, and relative transcript expression was calculated using the $2^{\Delta\Delta Ct}$ method. Data acquisition and analysis were performed using Bio-Rad CFX Maestro Software. Primer sequences are provided in Supplementary Table S5.

Bulk RNAseq data analysis

Total RNA was isolated from CM-Mito^{Miro1KO} and control mouse hearts (n=3 per group) using TRIzol reagent, and RNA integrity was assessed using an Agilent Bioanalyzer. cDNA libraries were generated and sequenced on an Illumina HiSeq 2500 V4 platform by iGenSeq, Paris Brain Institute (Paris, France). Gene-level raw count data and sample metadata were imported into R for downstream analysis.

For differential expression analysis, the groups were analyzed using DESeq2. Genes were retained when their counts per million (CPM) were ≥1 in at least three samples. Differential expression between CM-Mito^{Miro1KO} and control hearts was assessed using the Wald test, and P values were adjusted for multiple testing using the Benjamini–Hochberg method. Genes with an adjusted P value (FDR) <0.05 and an absolute log2 fold change (|log2FC|) ≥ 1 were considered differentially expressed.

GSEA was performed using the clusterProfiler R package with the fgsea algorithm. Native mouse gene sets were obtained from the Molecular Signatures Database (MSigDB) using the msigdbr R package. Gene sets containing 10–500 genes were tested, and P values were adjusted using the Benjamini–Hochberg method.

Samples preparation for metabolomic.

Metabolomics analyses were performed in mouse cardiac fibroblasts isolated from control or CM-Mito^{Miro1KO} hearts at day 14 post-tamoxifen treatment and in human cardiac fibroblasts following 24 h of preconditioning with mitochondria derived from RL14 cells. Each mouse

sample consisted of at least 1.10^6 cardiac fibroblasts pooled from three hearts, whereas each human sample contained $0.5.10^6$ cardiac fibroblasts.

Metabolites were extracted using solution composed of 50% methanol, 30% acetonitrile (ACN) and 20% water. Extraction volume was normalized to the cell number, with 1 ml used for every million cells. After addition of extraction solution, samples were vortexed for 5 min at 4 °C and centrifuged at 16,000 g for 15 min at 4 °C. The supernatants were collected and stored at −80°C until analysis.

Targeted metabolomics by liquid chromatography–mass spectrometry (LC-MS)

LC/MS analyses were conducted using QExactive Plus Orbitrap mass spectrometer equipped with an Ion Max source and a HESI II probe coupled to a Dionex UltiMate 3000 UPLC system (Thermo). The 5 µl samples were injected onto a ZIC-pHILIC column (150 mm × 2.1 mm; i.d. 5 µm) with a guard column (20 mm × 2.1 mm; i.d. 5 µm) (Merck) for LC separation. Buffer A was 20 mM ammonium carbonate, 0.1% ammonium hydroxide (pH 9.2), and buffer B was ACN. The chromatographic gradient was run at a flow rate of 0.2 µl min−1 as follows: 0–20 min, linear gradient from 80% to 20% of buffer B; 20–20.5 min, linear gradient from 20% to 80% of buffer B; 20.5–28 min, 80% buffer B. The mass spectrometer was operated in full scan, polarity switching mode with the spray voltage set to 2.5 kV and the heated capillary held at 320 °C. The sheath gas flow was set to 20 units, the auxiliary gas flow to 5 units and the sweep gas flow to 0 units. The metabolites were detected across a mass range of 75–1000 m/z at a resolution of 35,000 (at 200 m/z) with the automatic gain control target at 106 and the maximum injection time at 250 ms. Lock masses were used to ensure mass accuracy below 5 ppm. Data were acquired with Xcalibur software (Thermo). The peak area of metabolites was determined using TraceFinder software (Thermo), identified by the exact mass of each singly charged ion and by the known retention time on the HPLC column.

Metabolomics data analysis

Metabolomics data were processed and analysed in R using RStudio. Metabolite features were filtered by interquartile range, with the lowest 5% of features removed. For in vivo samples, no sample-wise normalization was applied because normalization was performed during sample extraction by adjusting the extraction volume according to the input amount. In vitro samples were normalized by sample median. Both datasets were then subjected to generalized log2 transformation and autoscaling. Pathway enrichment analysis was performed using the MetaboAnalystR package with the SMPDB pathway library, using the *Mus musculus* and *Homo*

sapiens libraries for the *in vivo* and *in vitro* datasets, respectively [58]. Pathway enrichment was calculated using the Global Test with relative-betweenness centrality for pathway topology.

Seahorse analysis

Cardiac fibroblasts were seeded at the density of 20 10^3 cells/well in 96 well plates. After 24 h exposure to RL14-derived mitochondria, cells were washed several times with PBS to remove extracellular cardiac mitochondria before analysis with a Seahorse XF Analyzer 24 V7.

OCR measurements were performed in XF RPMI media (Agilent, Cat#10-357-6100) supplemented with 10 mM glucose (Seahorse XF, Cat#103577-100), 2 mM of L-glutamine (Agilent, Cat#10-357-9100) and 1 mM sodium pyruvate (Agilent, Cat#10-357-8100). The cellular bioenergetics profile was evaluated using the Agilent Seahorse XF Cell Mito Stress Test, with sequential additions of 1 µM oligomycin (Sigma-Aldrich, Cat#O4876), an inhibitor of ATP synthase, 1 µM of the uncoupling agent, carbonyl cyanide 4-(trifluoromethoxy) phenylhydrazone (FCCP, Sigma-Aldrich, Cat#C2920) and 200 nM rotenone (Sigma-Aldrich, Cat#R8875) and 200 nM antimycin A (Sigma-Aldrich, Cat#A8674) to inhibit complex I and complex III of the respiratory chain, respectively.

Baseline cellular OCR was initially obtained from which basal respiration was derived by subtracting non-mitochondrial respiration following addition of ROT/AA. ATP-linked respiration was calculated by subtracting the oligomycin rate from baseline cellular OCR. Proton leak respiration was calculated by subtracting non-mitochondrial respiration from the oligomycin rate. Maximal respiratory capacity was derived by subtracting non-mitochondrial respiration from the FCCP rate. Mitochondrial reserve capacity was calculated by subtracting basal respiration from maximal respiratory capacity. Coupling efficiency was determined by calculating the percentage of OCR immediately following the oligomycin treatment over the final baseline value. At the end of the assay, the cells in the wells were lysed with RIPA buffer (Thermo Scientific, Cat#89900) and protein quantifications were made using the Pierce™ protein assay kit (Thermo Scientific, Cat#23227) based on the bicinchoninic acid (BCA) method. Results were analyzed using Seahorse Wave Desktop Software (Agilent) and were normalized by protein content.

Mitochondrial Complex activities measurements

Mitochondrial complex I- and complex II-dependent respiration was assessed in control and mitochondria-treated fibroblasts using a Seahorse XF Analyzer. Cells were maintained intact throughout the assay, without permeabilization, using cell-permeable succinate (MitoKit-

CII/Succinate-nv, 60201-01; Oroboros Instruments), as previously described [22]. Oxygen consumption was measured following sequential additions of rotenone (0.2 µM) to inhibit complex I, cell-permeable succinate (500 µM) to stimulate complex II-dependent respiration and antimycin A (0.2 µM) to inhibit complex III.

Complex I-dependent respiration was calculated as the difference between basal oxygen consumption rate (OCR) and OCR following rotenone addition. Complex II-driven respiration was calculated as the difference between OCR following succinate addition and OCR following antimycin A addition.

Statistical analysis

Statistical analyses were performed using GraphPad Prism 10.0 (GraphPad Software). Data are presented as mean ± SEM. For datasets with $n \geq 5$ independent experiments, normality and equality of variances of populations were assessed using the Shapiro–Wilk and Brown–Forsythe tests, respectively. Gaussian distributed data with equal variances were analyzed using unpaired two-tailed Student's *t*-test or one-way ANOVA, as appropriate; Welch's *t*-test or Welch's ANOVA was used when variances were unequal. Non-parametric data were analyzed using the Mann–Whitney *U*-test or Kruskal–Wallis test, as appropriate. For datasets with $n < 5$, non-parametric tests were used.

For metabolomics analysis, two-sided unpaired Welch's t-tests were used for comparisons between experimental groups.

The statistical test used for each analysis, sample size and *P* values are reported in the corresponding figure legends. Results are considered significant when $P < 0.05$.

For *in vivo* experiments, mice were randomly assigned to treatment groups for mitochondria transplantation experiments or echocardiographic analyses. Investigators were blinded to treatment allocation during experimentation, data acquisition, and data analysis. No statistical method was used to predetermine the sample size.

The authors declare no conflict of interest.

ACKNOWLEDGEMENTS

We thank Maria Mihoc and PECMV platform (UMS28, Sorbonne University, Paris) for *in vivo* experiments, Jacqueline Gao-Li for the genotyping of mice and Pierre Joanne for his contributions to the figures created using BioRender.

AMR was supported by Agence de la Biomédecine (24GREFFE019), ANR (ANR-20-CE18-0035-01). JSVG were supported by the fellowship from Fonds Marion Elizabeth Brancher. OA and ZL were supported by the AFM-Téléthon (Contract No.: 22142 and 28597).

The authors declare no conflict of interest.

AUTHOR CONTRIBUTIONS

JSVG performed co-culture experiments, mitochondria preconditioning of cardiac fibroblasts, and most of the associated *in vitro* experiments, and contributed to the *in vivo* studies.
ZL generated the transgenic mouse model, contributed to the design and analysis of *in vivo* studies, and participated in manuscript writing. AS performed mitochondria isolation and associated experiments and contributed to cardiac fibroblast isolation from mouse hearts. ZB interpreted RNA-sequencing and metabolomics data. GVA contributed to the analysis of in *vivo* mitochondria transplantation experiments. GR performed and analyzed RT-qPCR experiments. NG performed echocardiography and mitochondria transplantation via mouse tail vein injection. MF performed *in vivo* flow cytometry analyses. IN generated metabolomics data. SD performed *in vivo* immunohistochemistry experiments. AP prepared the protocols for mouse procedures for approval by the local Animal Ethics Committee of the Sorbonne University, Paris, France. MG performed tissue clearing and immunostaining experiments. IX designed the metabolomics experiments and developed the analytical methodology. OA contributed to experimental design and manuscript writing. A.M.R. conceived and designed the research and wrote the manuscript. All authors reviewed and approved the final manuscript.

REFERENCES

1. Pellman, J., Zhang, J. & Sheikh, F. Myocyte-fibroblast communication in cardiac fibrosis and arrhythmias: Mechanisms and model systems. *J Mol Cell Cardiol* **94**, 22–31 (2016).
2. Van Linthout, S., Matz, I., González, A. & Davis, J. Cardiac fibroblasts in myocardial injury and heart failure. *Eur Heart J* **47**, 2271–2285 (2026).
3. Chen, Z.-T. *et al.* Glycolysis Inhibition Alleviates Cardiac Fibrosis After Myocardial Infarction by Suppressing Cardiac Fibroblast Activation. *Front Cardiovasc Med* **8**, 701745 (2021).
4. Han, B. *et al.* PFKFB3 Promotes Myofibroblast Differentiation and Cardiac Fibrosis Through its Intra- and Extra- Cellular Roles. *J Cardiovasc Transl Res* **18**, 1353–1370 (2025).

5. Tian, G. *et al.* Voltage-dependent anion channel 1 (VDAC1) overexpression alleviates cardiac fibroblast activation in cardiac fibrosis via regulating fatty acid metabolism. *Redox Biol* **67**, 102907 (2023).
6. Rajesh, R. *et al.* Succinate aggravates pulmonary fibrosis through the succinate/SUCNR1 axis. *Am J Physiol Lung Cell Mol Physiol* **328**, L671–L684 (2025).
7. Wang, Z. *et al.* Pharmaceutical targeting of succinate dehydrogenase in fibroblasts controls bleomycin-induced lung fibrosis. *Redox Biol* **46**, 102082 (2021).
8. Park, S. Y., Le, C. T., Sung, K. Y., Choi, D. H. & Cho, E.-H. Succinate induces hepatic fibrogenesis by promoting activation, proliferation, and migration, and inhibiting apoptosis of hepatic stellate cells. *Biochem Biophys Res Commun* **496**, 673–678 (2018).
9. Xu, B. *et al.* Succinate links TCA cycle dysfunction to inflammation by activating HIF-1α signaling in acute kidney injury. *Int Immunopharmacol* **161**, 115105 (2025).
10. Wang, J., Yin, J., Liu, X., Liu, Y. & Jin, X. Gut commensal bacterium Bacteroides vulgatus exacerbates helminth-induced cardiac fibrosis through succinate accumulation. *PLoS Pathog* **21**, e1013069 (2025).
11. Wang, Z. *et al.* Succinate-driven PKM2 succinylation and dimerization accelerates age-associated cardiac fibrosis. *Commun Biol* **9**, 633 (2025).
12. Hall, C., Gehmlich, K., Denning, C. & Pavlovic, D. Complex Relationship Between Cardiac Fibroblasts and Cardiomyocytes in Health and Disease. *J Am Heart Assoc* **10**, e019338 (2021).
13. Brestoff, J. R. *et al.* Intercellular Mitochondria Transfer to Macrophages Regulates White Adipose Tissue Homeostasis and Is Impaired in Obesity. *Cell Metab* **33**, 270-282.e8 (2021).
14. Brestoff, J. R. *et al.* Recommendations for mitochondria transfer and transplantation nomenclature and characterization. *Nat Metab* https://doi.org/10.1038/s42255-024-01200-x (2025) doi:10.1038/s42255-024-01200-x.
15. Cai, W. *et al.* Mitochondrial Transfer Regulates Cell Fate Through Metabolic Remodeling in Osteoporosis. *Adv Sci (Weinh)* **10**, e2204871 (2023).
16. Dong, L.-F. *et al.* Mitochondria on the move: Horizontal mitochondrial transfer in disease and health. *J Cell Biol* **222**, e202211044 (2023).
17. Levoux, J. *et al.* Platelets Facilitate the Wound-Healing Capability of Mesenchymal Stem Cells by Mitochondrial Transfer and Metabolic Reprogramming. *Cell Metab* **33**, 283-299.e9 (2021).
18. He, K. *et al.* Long-distance intercellular connectivity between cardiomyocytes and cardiofibroblasts mediated by membrane nanotubes. *Cardiovasc Res* **92**, 39–47 (2011).
19. Song, R. *et al.* Cytoskeletal remodeling promotes tunneling nanotube formation and drives cardiac resident cell mitochondrial transfer in sepsis. *Sci Adv* **12**, eadz3266 (2026).
20. Iverson, T. M., Singh, P. K. & Cecchini, G. An evolving view of complex II-noncanonical complexes, megacomplexes, respiration, signaling, and beyond. *J Biol Chem* **299**, 104761 (2023).
21. Kang, S., Antoniewicz, M. R. & Hay, N. Metabolic and transcriptomic reprogramming during contact inhibition-induced quiescence is mediated by YAP-dependent and YAP-independent mechanisms. *Nat Commun* **15**, 6777 (2024).
22. Ehinger, J. K. *et al.* Cell-permeable succinate prodrugs bypass mitochondrial complex I deficiency. *Nat Commun* **7**, 12317 (2016).
23. Brière, J.-J. *et al.* Mitochondrial succinate is instrumental for HIF1alpha nuclear translocation in SDHA-mutant fibroblasts under normoxic conditions. *Hum Mol Genet* **14**, 3263–3269 (2005).
24. Rosina, M. *et al.* Ejection of damaged mitochondria and their removal by macrophages ensure efficient thermogenesis in brown adipose tissue. *Cell Metab* **34**, 533-548.e12 (2022).

25. Davis, C. O. *et al.* Transcellular degradation of axonal mitochondria. *Proc Natl Acad Sci U S A* **111**, 9633–9638 (2014).
26. Hayakawa, K. *et al.* Transfer of mitochondria from astrocytes to neurons after stroke. *Nature* **535**, 551–555 (2016).
27. Zhou, J. *et al.* Astrocytic LRP1 enables mitochondria transfer to neurons and mitigates brain ischemic stroke by suppressing ARF1 lactylation. *Cell Metab* **36**, 2054-2068.e14 (2024).
28. Ding, P. *et al.* Mitochondria from osteolineage cells regulate myeloid cell-mediated bone resorption. *Nat Commun* **15**, 5094 (2024).
29. Nicolás-Ávila, J. A. *et al.* A Network of Macrophages Supports Mitochondrial Homeostasis in the Heart. *Cell* **183**, 94-109.e23 (2020).
30. Baudo, G. *et al.* Polymer-Functionalized Mitochondrial Transplantation to Fibroblasts Counteracts a Pro-Fibrotic Phenotype. *Int J Mol Sci* **24**, 10913 (2023).
31. Kornicka-Garbowska, K., Groborz, S., Lynda, B., Galuppo, L. & Marycz, K. Mitochondria transfer restores fibroblasts-like synoviocytes (FLS) plasticity in LPS-induced, in vitro synovitis model. *Cell Commun Signal* **20**, 137 (2022).
32. Lee, S.-E. *et al.* Mitochondrial Transplantation Ameliorates Pulmonary Fibrosis by Suppressing Myofibroblast Activation. *Int J Mol Sci* **25**, 12783 (2024).
33. Cangkrama, M. *et al.* MIRO2-mediated mitochondrial transfer from cancer cells induces cancer-associated fibroblast differentiation. *Nat Cancer* **6**, 1714–1733 (2025).
34. Liu, T. *et al.* Transfer of Damaged Mitochondria from Cancer Cells to Cancer-Associated Fibroblasts Promotes Tyrosine Kinase Inhibitor Tolerance in EGFR-Mutant Lung Cancer. *Cancer Res* **86**, 1215–1231 (2026).
35. Datar, Y., Chaffin, M., Simonson, B., Mandia, A. & Ellinor, P. T. An integrated cell atlas of 2.4 million cardiac cells across 209 individuals in health and disease. *Nat Cardiovasc Res* **5**, 624–637 (2026).
36. Farah, E. N. *et al.* Spatially organized cellular communities form the developing human heart. *Nature* **627**, 854–864 (2024).
37. Litviňuková, M. *et al.* Cells of the adult human heart. *Nature* **588**, 466–472 (2020).
38. Patrick, R. *et al.* Integration mapping of cardiac fibroblast single-cell transcriptomes elucidates cellular principles of fibrosis in diverse pathologies. *Sci Adv* **10**, eadk8501 (2024).
39. Zamberlan, M. & Semenzato, M. Mechanisms of Mitochondrial Transfer Through TNTs: From Organelle Dynamics to Cellular Crosstalk. *Int J Mol Sci* **26**, 10581 (2025).
40. Mahrouf-Yorgov, M. *et al.* Mesenchymal stem cells sense mitochondria released from damaged cells as danger signals to activate their rescue properties. *Cell Death Differ* **24**, 1224–1238 (2017).
41. Ahmad, T. *et al.* Miro1 regulates intercellular mitochondrial transport & enhances mesenchymal stem cell rescue efficacy. *EMBO J* **33**, 994–1010 (2014).
42. Babenko, V. A. *et al.* Miro1 Enhances Mitochondria Transfer from Multipotent Mesenchymal Stem Cells (MMSC) to Neural Cells and Improves the Efficacy of Cell Recovery. *Molecules* **23**, 687 (2018).
43. Lin, Y.-H. *et al.* Miro1 improves the exogenous engraftment efficiency and therapeutic potential of mitochondria transfer using Wharton's jelly mesenchymal stem cells. *Mitochondrion* **76**, 101856 (2024).
44. Zhao, F. *et al.* Miro1-mediated mitochondrial transfer boosts stem cell therapy for muscle atrophy via restoring mitochondrial homeostasis. *Stem Cell Res Ther* https://doi.org/10.1186/s13287-026-05191-2 (2026) doi:10.1186/s13287-026-05191-2.
45. Novak, J. *et al.* The adaptor protein Miro1 modulates horizontal transfer of mitochondria in mouse melanoma models. *Cell Rep* **44**, 115154 (2025).
46. Saha, T. *et al.* Intercellular nanotubes mediate mitochondrial trafficking between cancer and immune cells. *Nat Nanotechnol* **17**, 98–106 (2022).

47. Tannahill, G. M. *et al.* Succinate is an inflammatory signal that induces IL-1β through HIF-1α. *Nature* **496**, 238–242 (2013).
48. Tseng, P.-L. *et al.* Decreased succinate dehydrogenase B in human hepatocellular carcinoma accelerates tumor malignancy by inducing the Warburg effect. *Sci Rep* **8**, 3081 (2018).
49. Shin, B. *et al.* A Novel Biological Strategy for Myocardial Protection by Intracoronary Delivery of Mitochondria: Safety and Efficacy. *JACC Basic Transl Sci* **4**, 871–888 (2019).
50. Celik, A. *et al.* Revitalizing donor organs: The potential of mitochondrial transplantation in heart and lung transplantation. *J Heart Lung Transplant* **44**, 1648–1658 (2025).
51. Conejeros, C., Parra, V., Sanchez, G., Pedrozo, Z. & Olmedo, I. Miro1 as a novel regulator of hypertrophy in neonatal rat cardiomyocytes. *J Mol Cell Cardiol* **141**, 65–69 (2020).
52. Froese, N. *et al.* RHOT Proteins Link Mitochondrial Motility to Cardiomyocyte Sarcomere Maturation. *Circ Res* **138**, e327297 (2026).
53. Kassab, S. *et al.* Loss of Miro1 drives cardiac and mitochondrial dysfunction exacerbated by metabolic stress. *J Mol Cell Cardiol* S0022-2828(26)00122–7 (2026) doi:10.1016/j.yjmcc.2026.08.004.
54. Lian, X. *et al.* Directed cardiomyocyte differentiation from human pluripotent stem cells by modulating Wnt/β-catenin signaling under fully defined conditions. *Nat Protoc* **8**, 162–175 (2013).
55. Maayah, Z. H., Elshenawy, O. H., Althurwi, H. N., Abdelhamid, G. & El-Kadi, A. O. S. Human fetal ventricular cardiomyocyte, RL-14 cell line, is a promising model to study drug metabolizing enzymes and their associated arachidonic acid metabolites. *J Pharmacol Toxicol Methods* **71**, 33–41 (2015).
56. Anunciado-Koza, R. V. P. *et al.* Purification of functional mouse skeletal muscle mitochondria using percoll density gradient centrifugation. *BMC Res Notes* **16**, 243 (2023).
57. Ackers-Johnson, M. *et al.* A Simplified, Langendorff-Free Method for Concomitant Isolation of Viable Cardiac Myocytes and Nonmyocytes From the Adult Mouse Heart. *Circ Res* **119**, 909–920 (2016).
58. Pang, Z. *et al.* MetaboAnalyst 6.0: towards a unified platform for metabolomics data processing, analysis and interpretation. *Nucleic Acids Res* **52**, W398–W406 (2024).

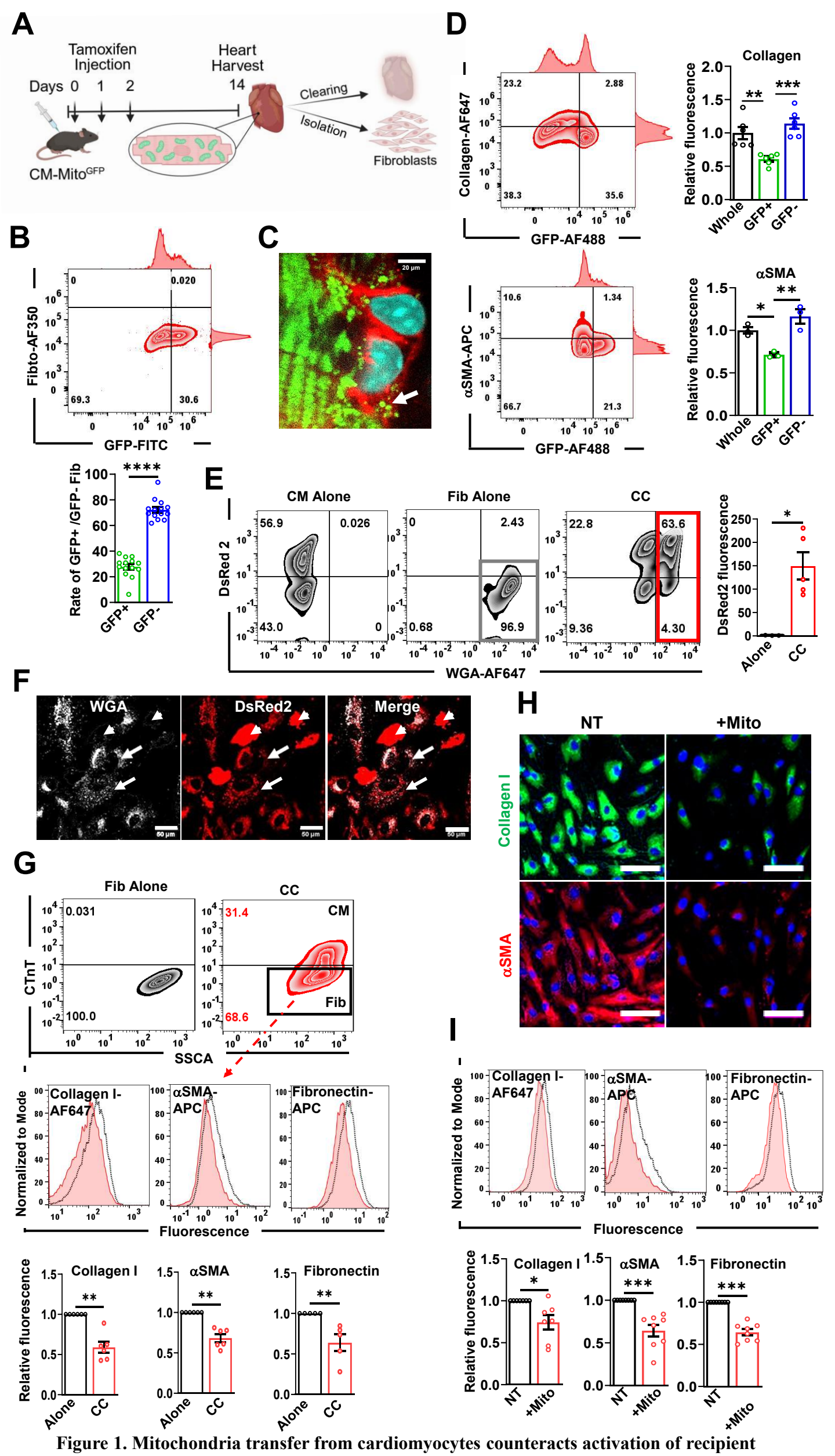


Figure 1. Mitochondria transfer from cardiomyocytes counteracts activation of recipient cardiac fibroblasts

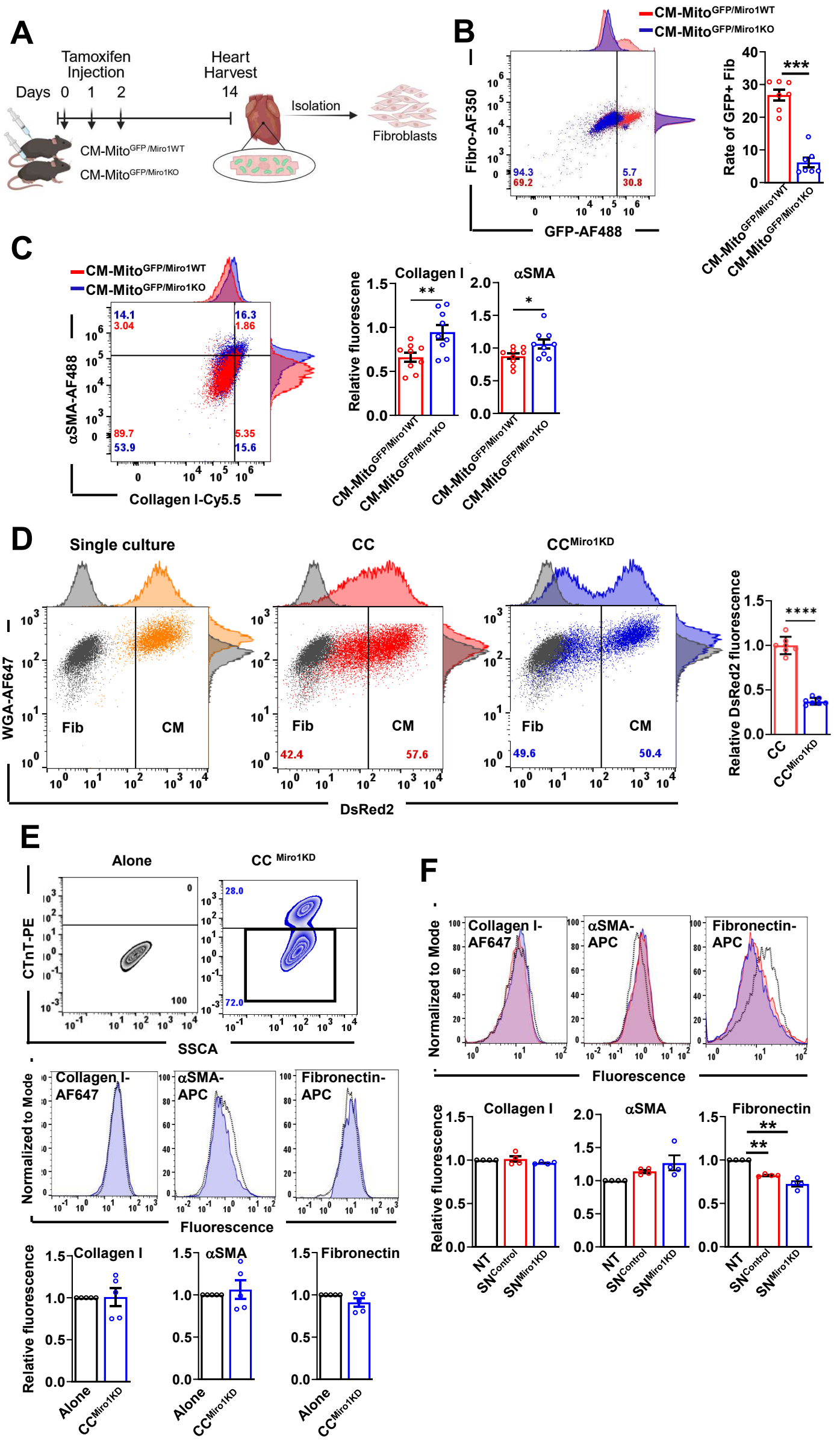


Figure 2. Miro1 facilitates mitochondria transfer from cardiomyocytes to cardiac fibroblasts and prevents profibrotic activation

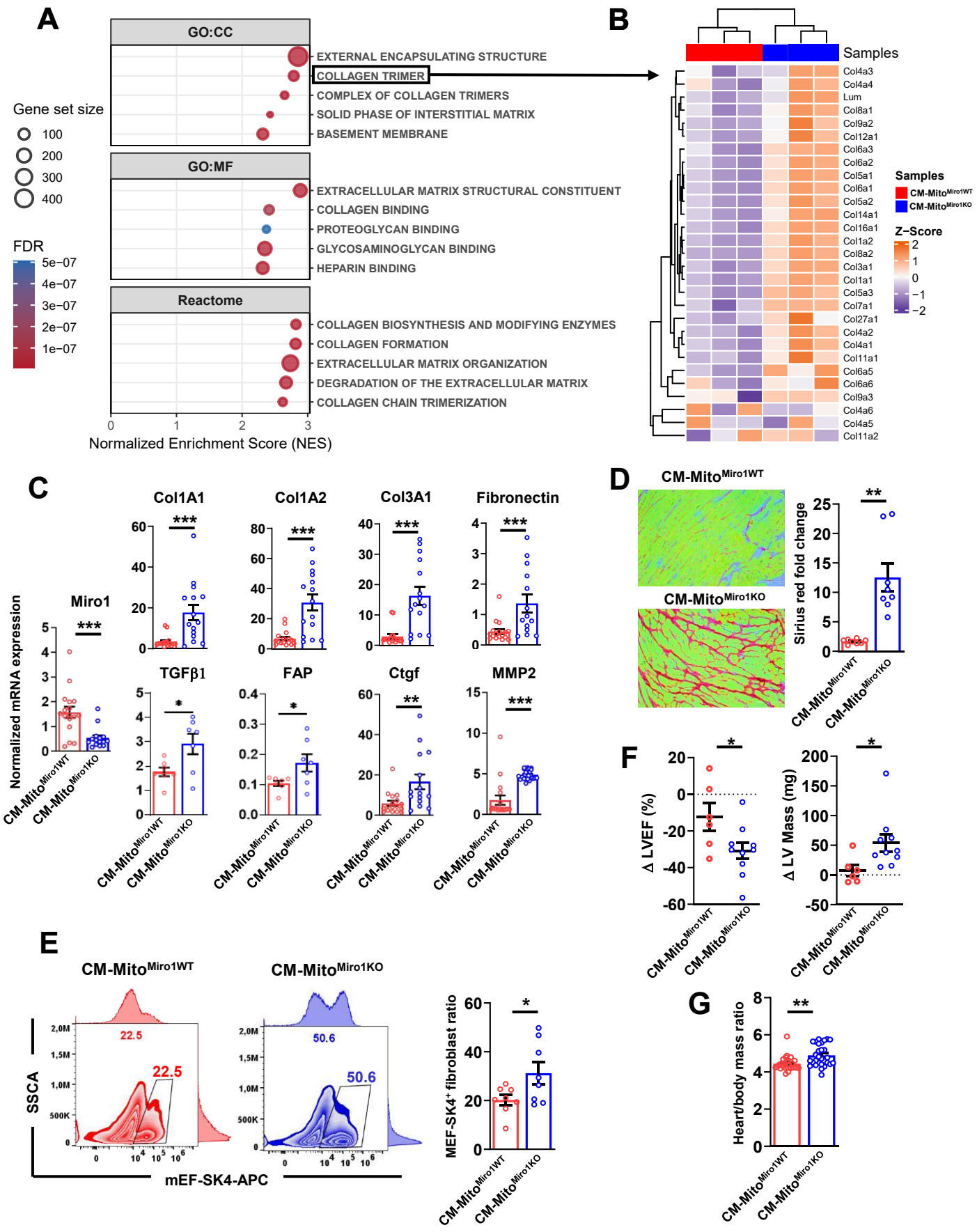


Figure 3: Silencing Miro1 in cardiomyocytes exacerbates fibrosis and impairs heart function

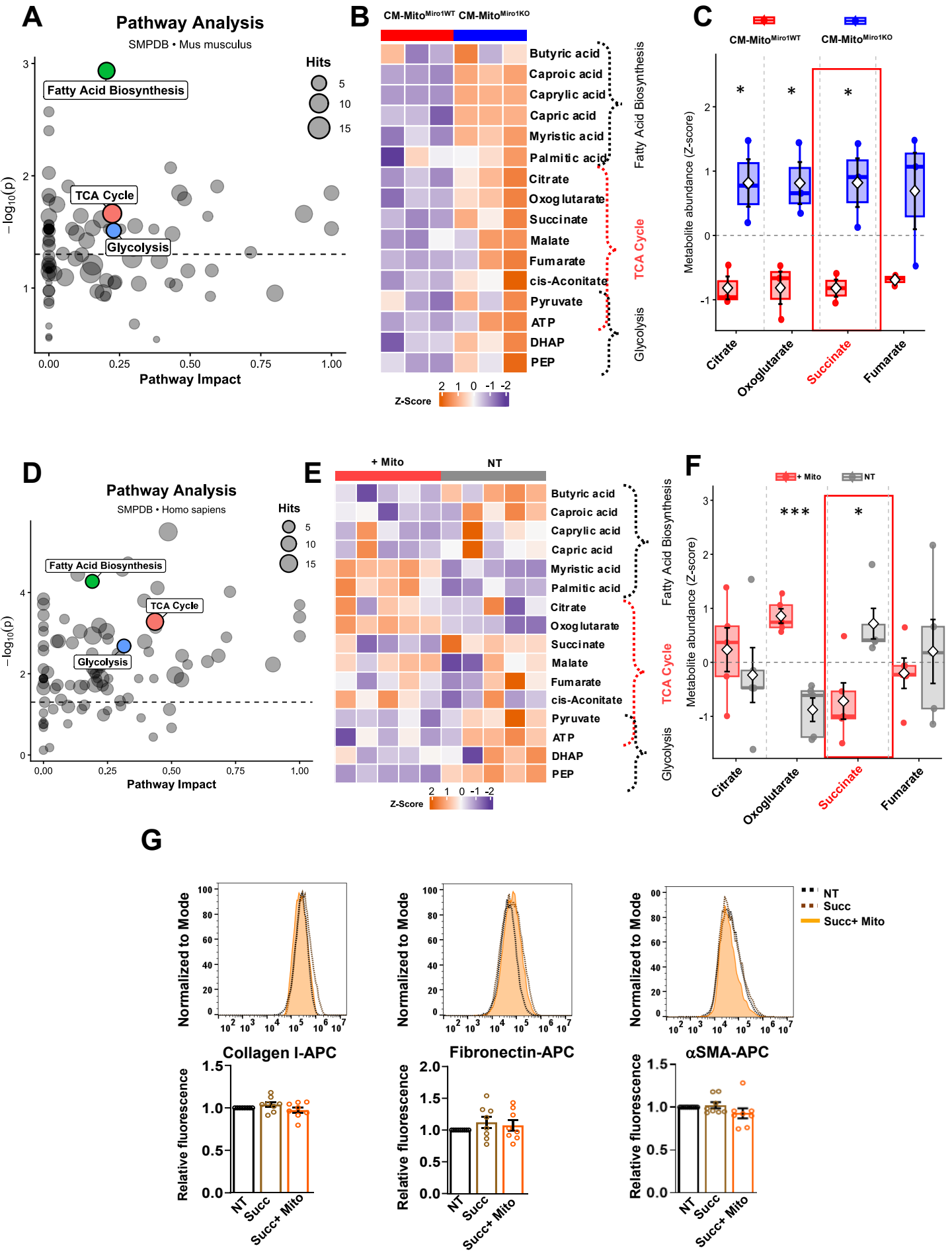


Figure 4. Mitochondria transfer from cardiomyocytes leads to decreased succinate levels in recipient cardiac fibroblasts.

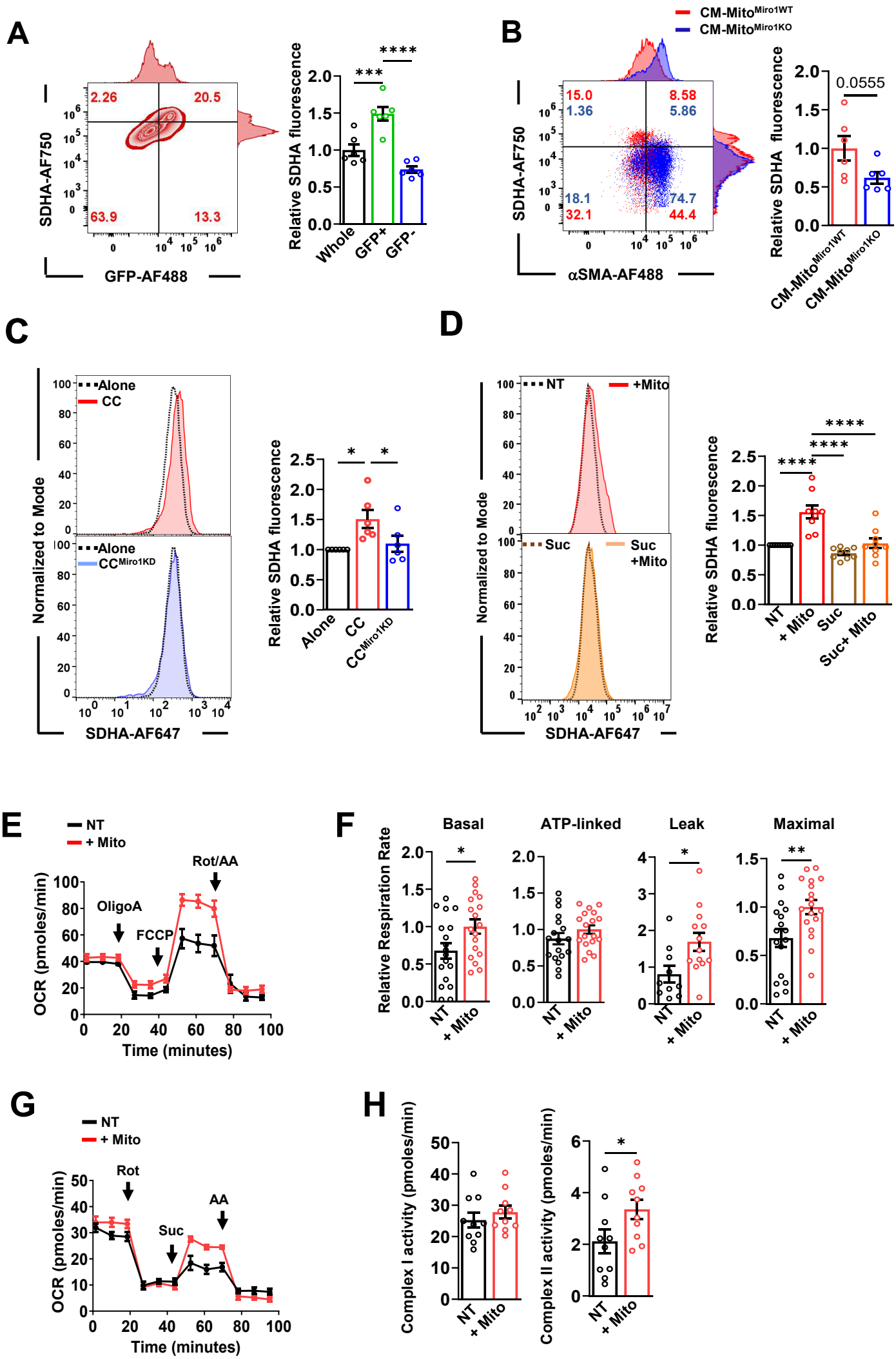


Figure 5. Mitochondria transfer from cardiomyocytes enhances mitochondria complex II expression in recipient cardiac fibroblasts.

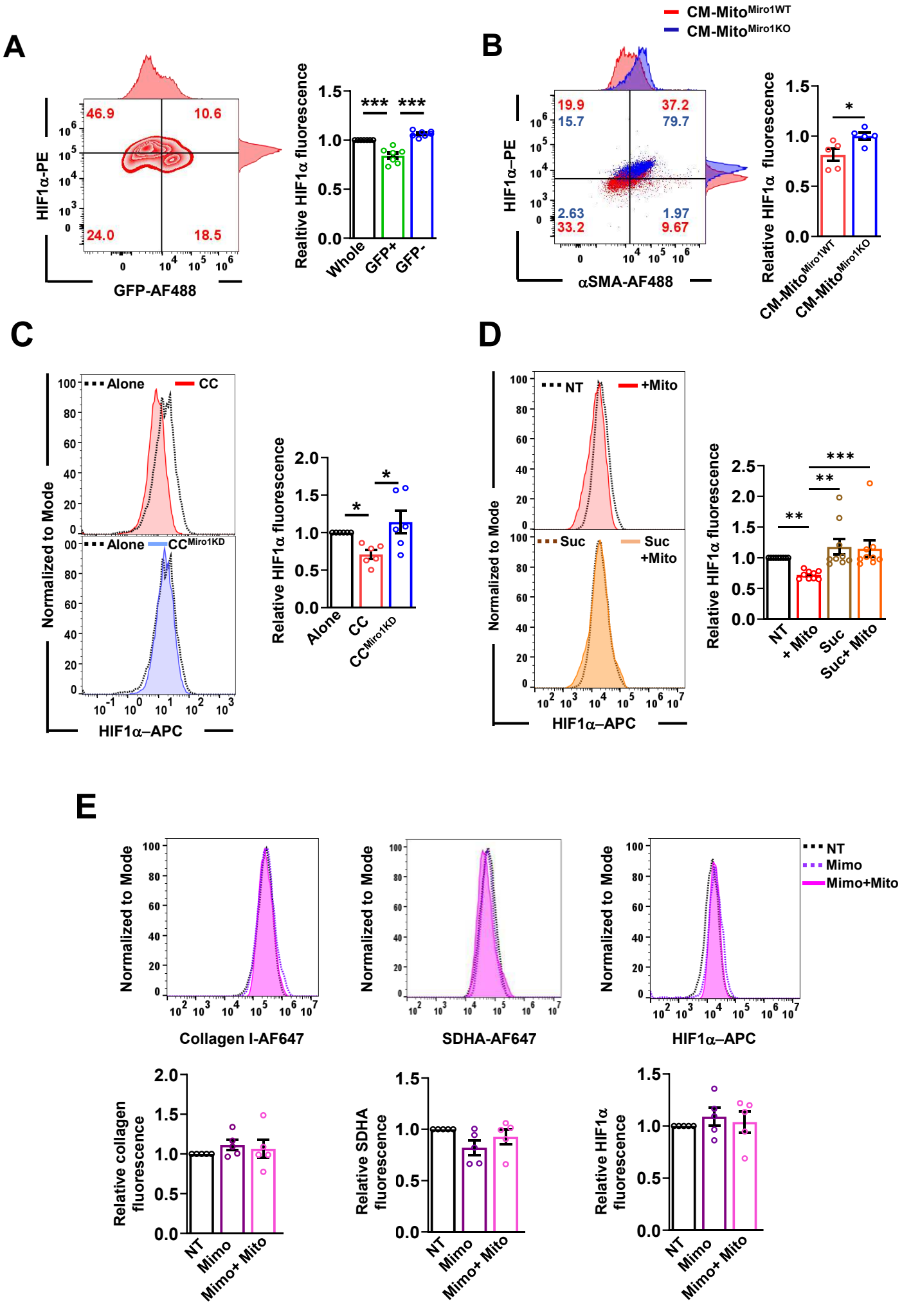


Figure 6. Mitochondria transfer from cardiomyocytes decreases HIF1a expression in recipient cardiac fibroblasts.

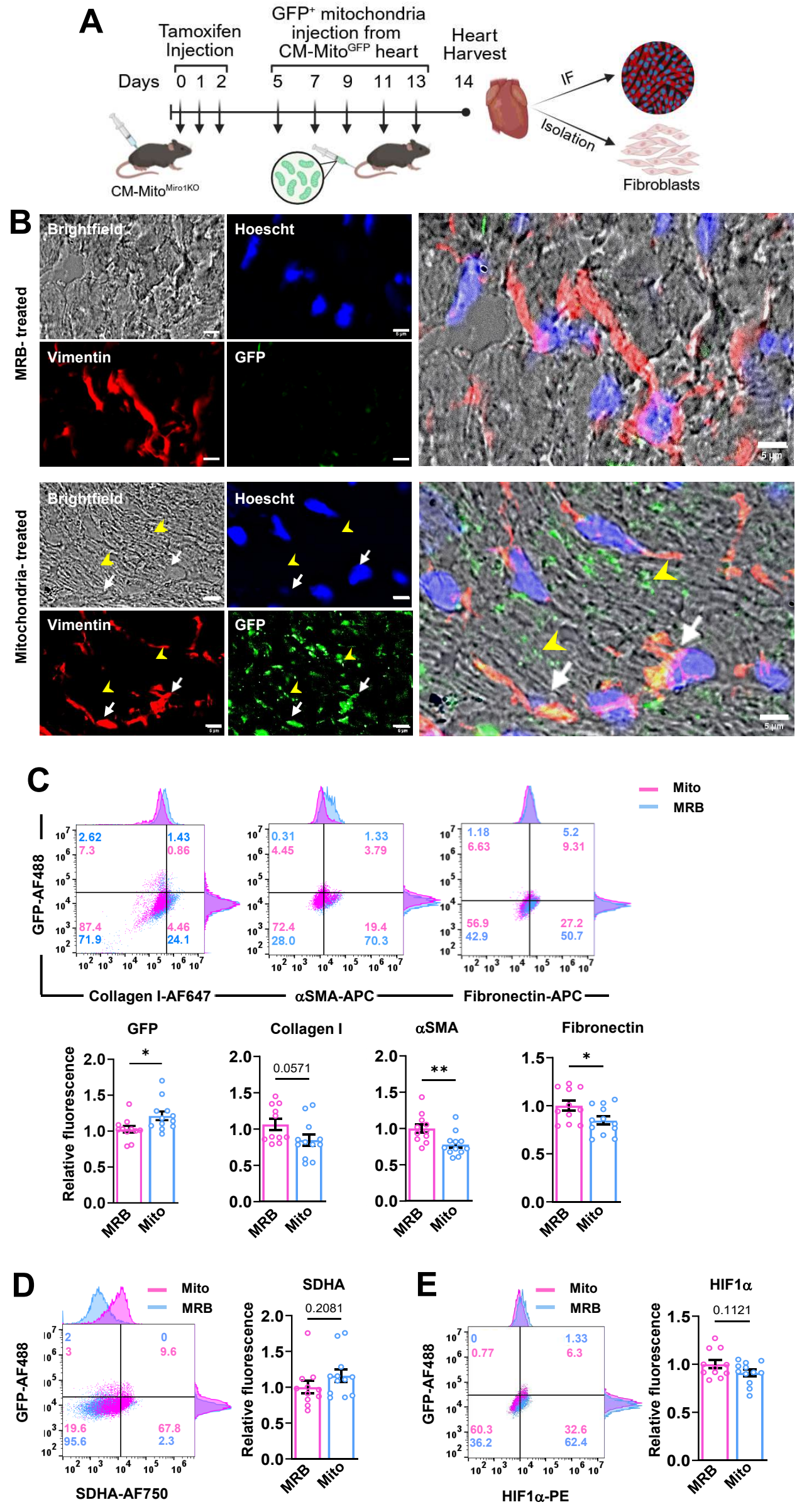


Figure 7. Mitochondria transplantation alleviates the pro-fibrotic phenotype of cardiac fibroblasts in CM-Mito^{Miro1KO} mice.

Supplementary Files

This is a list of supplementary files associated with this preprint. Click to download.

- SupplementaryTableS1DEGCMMitoMiro1KOvsMitoMiro1WTTPM.xlsx
- SupplementaryTableS4PathwayEnrichmentInVivoInVitro.xlsx
- SupplementaryTable5.pdf
- SupplementaryFigureS1S2.pptx
- SupplementaryTableS2GSEAGOCCMFReactomeMouseCMMitoMiro1KOvsMitoMiro1WT.xlsx
- SupplementaryTableS3IndividualMetabolitesInVivoInVitro.xlsx
- SupplementaryFigureS1S2S31.pdf